A MULTISCALE THEORY TO DETERMINE THERMODYNAMIC PROPERTIES OF CONFINED FLUIDS

BY

MOHAMMAD HOSSEIN MOTEVASELIAN

THESIS

Submitted in partial fulfillment of the requirements
for the degree of Master of Science in Mechanical Engineering
in the Graduate College of the
University of Illinois at Urbana-Champaign, 2015

Urbana, Illinois

Adviser:

Professor N. R. Aluru

ABSTRACT

Empirical potential-based quasi-continuum theory (EQT) provides a route to incorporate atomistic detail into a continuum framework such as the Nernst-Planck equation. EQT is a simple and fast approach to predict inhomogeneous density and potential profiles of confined fluids. EQT potentials can be used to construct a grand potential functional for classical density functional theory (cDFT). The combination of EQT and cDFT provides a robust and accurate approach to predict the structure and thermodynamic properties of confined fluids at multiple length-scales, ranging from few Angstroms to macro meters. In this work, first, we demonstrate the EQT-cDFT approach by simulating single component Lennard-Jones (LJ) fluids, namely, methane and argon, confined inside slit-like channels of graphene. For these systems, we show that the EQT-cDFT can accurately predict the structure and thermodynamic properties, such as density profiles, adsorption, local pressure tensor, surface tension, and solvation force of confined fluids as compared to the MD simulation results. Next, we extend the EQT-cDFT approach to confined fluid mixtures and demonstrate it by simulating a mixture of methane and hydrogen inside slit-like channels of graphene. We show that the EQT-cDFT predictions for the structure of the confined fluid mixture compare well with the MD simulations results. In addition, our results show that graphene slit nanopores exhibit a selective adsorption of methane over hydrogen.

Key Words: confined nanofluids, Empirical potential-based quasi-continuum theory (EQT), classical density functional theory (cDFT), molecular dynamics (MD), confined mixture, thermodynamic properties

To my parents, for their love and encouragement.
To my friends, for their help and support.

ACKNOWLEDGMENTS

I would like to express my deep gratitude to my advisor Prof. N. R. Aluru, who has challenged and guided me in the past three years. This work was done under his supervision. His insights into the research project, asking fundamental and focused questions, helped me to reach a better and fundamental understanding of my research project.

I would also like to thank S. Y. Mashayak, for his helpful discussions and patience for answering my numerous questions. I would like to acknowledge the financial support by NSF under grant Nos. 1264282, 1420882 and AFOSR under grant No. FA9550-12-1-0464.

I am deeply grateful to my parents who have raised me and always been supportive. They always encourage and trust me whatever situation or difficulty I encounter. It would not have been possible for me to come to this stage of my life without their unchanging love and unlimited support. Last but most importantly, I am grateful for believing the one who I owe all my success in life.

TABLE OF CONTENTS

CHAPTER 1

INTRODUCTION

1.1 Background and Motivation

For nearly all systems of interest to us, the most transferrable and fundamental description of matter is one that invokes quantum mechanics. Solving Schrödinger's equation for the system of interest, yields the highest level of accuracy. However, accounting for all subatomic particles in the system requires huge amount of computer resources. Moreover, depending on the system size, it is even impossible to approach a system quantum mechanically. Thus, many approximations need to be made in order to simplify the system and make it solvable for the computer. Ab initio methods, density functional theories are among such techniques that invoke approximations to make a system tractable for the computer. But, even these methods are limited only to a small number of atoms.

Sometimes we are interested in a physical phenomenon that manifest itself at larger time or length scales, so we do not need the fine-grained detail in order to understand them. In other words, we can coarse-grain fine details to run simulations longer than those achieved by the first-principle methods. On the other hand, there are examples such as protein folding and viral capsid assembly that the physical observables, which occur at large time and length scales, are highly connected to the details at the finer levels. Thus, there is a need for methods to link simulations hierarchy, namely multiscale modeling, shown in Fig. 1.1.

As shown in Fig. 1.1, there are two ways that the information can be propagated between the levels: i) bottom-up and ii) top-down. The top-down approach is to inform the finer levels by providing input from coarser levels. For example, inputs from experimental studies such as molecular structure can help to develop molecular models and different force-fields required for particle to interact. The bottom-up approach, however, tries to use information available at the all-atom level and incorporate them into a coarser level, so that the time and length scales are bridged from atomistic level all the way to the macroscopic level. Here in this thesis, we will introduce a multiscale approach, namely EQT, that allows study of system of multiple length-scales, ranging from few Angstroms to macro meters.

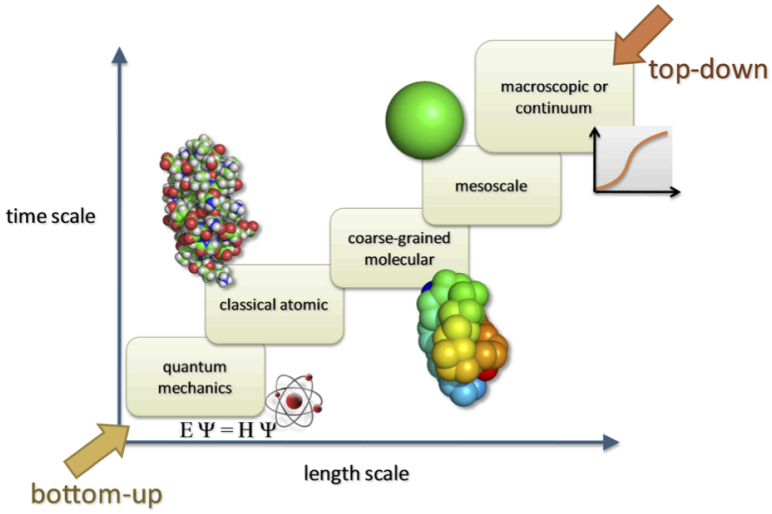

Figure 1.1: Hierarchy of simulations from sub-atomic level (quantum mechanics) to the macroscopic level (continuum approaches). (The figure is adopted from the "Coarse graining and multiscale techniques" lecture (ChE210D) by Scott Shell at UCSB.

Fluids and their mixtures in confined geometries ranging from nano- to micro-sized dimensions are interesting systems to study because of their appealing applications, such as nanofiltration [1, 2, 3, 4, 5], adsorption, lubrication [6], drug delivery [7], enhanced oil recovery [8, 9], heat management [10, 11], material synthesis [12], separations, and geophysical application [13]. In confinement, due to the spatial constraints and competition between the surface-fluid and fluid-fluid atomic interactions, the fluid properties can be significantly different from the bulk fluid. For example, the pressure experienced by a fluid confined in a nanopore can be orders of magnitude higher than the pressure in the bulk fluid [14]. Such unusual behavior of confined fluids can have practical applications, e.g., a carbon nanotube (CNT) can be used as a super-compressor for the synthesis of valuable high-pressure materials, such as KI nanocrystals [12]. In addition, the layering of fluid molecules near a wall has profound effects on the properties of confined fluids. For instance, the velocity profile of a nanoconfined fluid between two surfaces is strongly influenced by the density oscillations [15, 16]. Therefore, study of confined fluids is important to get atomic-level insights into their unusual properties and to enable the design of novel nanofluidic applications.

Over the past few decades, atomistic descriptions such as molecular dynamics (MD) and Monte Carlo (MC) simulations have been widely used to study fluids and their mixtures in nanoconfinement [13, 17]. However, it is computationally expensive to do full molecular simulations for systems involving multiple length- and time-scales ranging from the quantum to atomic to continuum scales. On the other hand, it has been shown that to study fluid-fluid or fluid-solid in-

terfaces, classical continuum descriptions fail to accurately capture atomistic details [18, 19]. To address these issues, we need a multiscale method which is not only as accurate as molecular simulations, but also as fast as classical continuum methods. In addition, the method should be computationally simple, especially when dealing with multi-component fluid systems.

1.2 Thesis Overview

This thesis provides a comprehensive computational study for Lennard-Jones fluids confined in slit-like channels from all-atom and continuum perspective by studying argon, methane and a binary mixture of hydrogen and methane molecules inside graphene slit nano channels. In this section, we provide the general layout of this thesis and briefly summarize its chapters.

Chapter 2 discusses the fundamentals of the molecular dynamics simulation, including the underlying algorithm, different ensembles and potentials used in MD simulations. In addition, the essential details about the MD simulation setups are provided for the case studies considered in this thesis.

Chapter 3 describes the fundamentals on the Emperical potential-based Quasi-Continuum Theory (EQT). We introduce EQT as a multiscale method that seamlessly integrate atomistic details into a continuum-based model. Moreover, to clarify the theory for the readers, a brief overview on particle densities and pair distributions is provided. Finally, the frame work is extended to account for the multi-component systems as well.

In chapter 4, the EQT potentials are used within the classical density functional theory (cDFT) in order to obtain thermodynamic properties other than the fluid structure. In this chapter, brief overview of the cDFT frame work is presented. Furthermore, necessary thermodynamic relations are derived and discussed.

In chapter 5, the EQT-cDFT results are provided and compared with the all-atom reference MD simulations. Various thermodynamic properties such as density profiles, adsorption, local pressure tensor, surface tension, and solvation force are predicted by the EQT-cDFT approach and compared with the MD simulation results.

Finally, chapter 6 summarizes the major accomplishments of the thesis and shows the possible future directions of the research.

CHAPTER 2

MOLECULAR DYNAMICS SIMULATION OF NANOCONFINED LENNARD-JONES FLUIDS

Nowadays, computer simulations are essential tools in scientific research. They serve as a complement to experiments, enabling us to understand and further develop systems that are not even experimentally feasible in laboratory. In some cases experiments are impossible to do, too dangerous, expensive or even blind for properties that cannot be observed on short time- and very small space-scales. Under these circumstances, one can cling on computer simulations to circumvent the practical problems exist in experiments.

2.1 Fundamentals of MD simulation

The underlying physics of Molecular Dynamics (MD) simulation are Newton's law of motion. At any time, for an N particle system, position ($\mathbf{r}^N$) and momentum ($\mathbf{p}^N$) are two key variables to determine the state of the entire system. For a system of particles to evolve in time, we need to be able to calculate forces ($\mathbf{F}_i$) on each particle. In MD, atoms and molecules are allowed to interact based on some potential function that is usually called force field. The knowledge of force field is based on finer theories such as quantum mechanics, which allow one to determine the interactions from the first principles. Once the force field is determined, the governing Newton's equation of motion can be integrated to create trajectories and velocities using a suitable numerical algorithm (i.e. Verlet Algorithm). The following flowchart summarizes the necessary steps for performing classical molecular dynamics simulations.

1) Input initial conditions (potential interaction, V, as a function of atom positions, positions $\mathbf{r}$ and velocities $\mathbf{v}$ of all atoms in the system).

2) Repeat 3,4,5 for the required number of steps.

3) Compute forces on each atom based on the potential and any external forces exerting on the system.

4) Update positions and velocities of the atoms based on calculations in step 3.

5) Outputting quantities such as positions, velocities, forces and analyzing trajectories for desired static and dynamic properties.

1. **System initialization**

In order to start the simulation in MD, it is necessary to construct a molecular model consisting N number of particles. Initially, positions and velocities should be assigned to all particles. The particle positions should be chosen such that they do not overlap on each other; otherwise it will result in unrealistic forces, causes the simulation to crash. In order to avoid this problem, one can initially place the particles on a cubic lattice [20] and perform energy minimization algorithms to minimize the potential within the specified tolerance. Among all the algorithms, steepest decent method is the popular one due to its robustness and ease of implementation [21].The initial velocities are taken from a Maxwellian distribution at the given temperature. The temperature of the system can be monitored using the equipartion theory:

$$T = \frac{1}{k_B N_{\text{dof}}} \sum_{i=1}^{N} m(v_x^2 + v_y^2 + v_z^2) \tag{2.1}$$

where k_B is the Boltzmann constant, m is the particle mass and N_{dof} is the number of degrees of freedom.

2. **Force calculation**

The force acting on a particle i is computed by $\mathbf{F}_i = \partial V/\partial \mathbf{r}_i$, where V is the potential energy of the system. Basically, the interaction between atoms and molecules is determined from quantum mechanics, where one can get rid of electrons and consider the effective interaction of nuclei- the potential energy surface, V. To calculate V there are methods such as quantum chemistry, Ab initio and semi-empirical approach. In semi-empirical approach people try to make a good guess and use experimental data or quantum calculations to adjust it. This method is fast and it is widely used in classical MD, but depending on the complexity of the potential surface it may not reveal correct details. In quantum chemistry approach potential surface is computed at a few points and fitted to a reasonable form. The method is hard, due to its complexity and computational effort. Finally, in Ab initio, quantum calculations are performed on the fly as the trajectory being generated. This procedure couples quantum calculation of the electrons with classical one of the nuclei. It requires more computational effort; however, no analytical form is needed. Force calculation is the most time consuming step in the MD simulation (time required to calculate the forces on N particles in the system scales as $O(N^2)$. However, there are efficient algorithms that would ensure that force calculation is done in the order of $O(N(lnN))$.

3. **Integrating the equation of motion**

A ubiquitous choice of integrator in MD simulations is the Verlet algorithm. One can Taylor expand the position at time $t + \Delta t$ and $t - \Delta t$.

$$r(t+h) = r(t) + v(t)h + \frac{1}{2}a(t)h^2 + b(t)h^3 + O(h^4), \tag{2.2a}$$

$$r(t-h) = r(t) - v(t)h + \frac{1}{2}a(t)h^2 - b(t)h^3 + O(h^4), \tag{2.2b}$$

where r is the coordinate of the particle, $a(t)$ is the acceleration of the particle at time t, $b(t)$ is the third derivative of the position with respect to time, Δt is the time step in the MD simulation, v is the particle velocity, and m represents the mass of the particle. Adding Eqs. 2.2a and 2.2b, new positions in the Verlet algorithm can be obtained as

$$r(t+h) = 2r(t) - r(t-h) + \frac{f(t)}{m}h^2 + O(h^4) \tag{2.3}$$

where we substitute acceleration by the force acting on the particle at time t divided by its mass. To estimate velocities, one can subtract Eq. 2.2b from Eq. 2.2a to get the new velocity from the following equation,

$$v(t) = \frac{r(t+h) - r(t-h)}{2h} + O(h^2) \tag{2.4}$$

We note that time reversal invariance is built in the Verlet algorithm. In other words, the energy does not drift either up or down and it is constant. Instead, if the temperature of the system is to be maintained constant, the update algorithm is modified depending on which thermostat is used. Two of the commonly used thermostats are the Berendsen [22] and the Nosé-Hoover thermostat [23].

The choice of time step Δt depends on both system and the quantity of interest, which is calculated from MD simulation [24]. Choosing a very small time step increases the cost of the simulation and may not be possible for systems containing large number of particles. On the other hand, increasing the time step is computationally preferable, but the resultant trajectories may be very different from the actual physical system. Therefore, the time step for MD simulation should be optimized for both speed and accuracy of the simulation.

4. **Output and data analyses**

In statistical mechanics, the ensemble average is defined as the average of a quantity weighted by a probability density distribution. A property, such as temperature, is calculated by averaging over the instantaneous properties of the fluctuating system. Each state can be microscopically different, but the ensemble average is a stable characterization of the system that results in a unique macroscopic variable. The ergodic hypothesis postulates that one can

make the implicit assumption that an ensemble average (which relates to many replicas of the system) is the same as an average over time of one replica (the system we are studying). Therefore, in MD, various properties and a of the system can be calculated by averaging trajectories over a long time interval. A classical example of such calculation is the self-diffusion coefficient, D, based on velocity auto correlation function [25] obtained from MD trajectories.

$$D = \frac{1}{3N} \int_0^\infty \left\langle \sum_{j=1}^{N} v_j(t_0) v_j(t) \right\rangle dt \tag{2.5}$$

Other relevant examples to this work such as density distributions and potential of mean force profiles will be discussed in detail in subsequent chapters.

2.1.1 Thermodynamic ensembles

As it was mentioned in Section 2.1, if the system is ergodic, ensemble averages can be replaced by time averages. Furthermore, in the Verlet algorithm number of particles (N), volume (V) and the energy (E) is constant. Therefore, time averaging in a conventional MD simulation is equivalent to ensemble averaging in microcanonical ensemble (NVE). However, it is difficult to maintain system energy constant in real experiments. It requires to perfectly isolating the system to avoid any heat or mass transfer with the surrounding. On the other hand, it is more convenient to work under constant temperature, pressure or volume. Hence, for MD to emulate such conditions, different ensembles are available to maintain the thermodynamic properties of interest. The various commonly used ensembles can be categorized as follows.

1) **Microcanonical Ensemble (NVE)**

Microcanonical ensemble statistically describes a system that is isolated (i.e. no energy exchange and mass transfer is allowed) from its surrounding and the particle number and volume of it are unchanged throughout the simulation. In this description, according to the Boltzmann each possible microstate of the system is equally probable. In reality, realizing such conditions is extremely hard. In the simulations especially for solids, one should be cautious about the choice of time step. Failure to choose an appropriate time step will result in energy drift in the simulation that violates the energy conservation. This can also be attributed to the incorrect preparation of the sample.

2) **Canonical Ensemble (NVT)**

Also called isochoric-isothermal ensemble, NVT is used to represent mechanical systems of constant volume that are in thermal equilibrium with an external heat bath. The relevant thermodynamic free energy for this ensemble is the Helmholtz free energy $F(= U - TS$, where U is the internal energy and S is the

entropy of the system). The use of thermostats enables MD simulations to maintain the average temperature of the system at a constant value. Various techniques to control temperature include Anderson [26], Berendsen, Nosé-Hoover and Langevin (stochastic) thermostats. In Anderson and Langevin thermostats, the temperature is held constant by a coupling mechanism between the system and external heat bath. The mechanism is based on introducing stochastic forces, which modify the kinetic energy of the atoms in order to steer temperature to the desired value. Since the momentum transfer is destroyed using these algorithms, Anderson and Langevin thermostats should not be used for dynamic properties such as diffusion [27]. In Berendsen thermostat velocities of the atoms rescaled frequently to control temperature. This procedure does not strictly follow the canonical ensemble and suffers from time-irreversibility problem. Finally in Nosé-Hoover thermostat there are no random forces or velocities to deal with. The idea is to modify the equation of motion using extended Lagrangian formalism. In this technique temperature is controlled by means of a friction factor that alter particle velocities in the simulation. Main advantages of Nosé-Hoover thermostat are time-reversibility and the fact that it does not alter the dynamics of the system.

3) **Isobaric-Isothermal Ensemble (NPT)**

This kind of ensemble is very useful in chemistry because it mimics the real conditions in experiments where the chemical reactions occur under the constant pressure [28]. The relevant thermodynamic potential for this ensemble is the Gibbs free energy $G(= F + PV)$. Similar to thermostats, to keep the average pressure constant barostats are used for this purpose. The most common among them are Berendsen and Parinello-Rahman barostats [21]. The former is usually used to pre-equilibrate the system while the latter is useful to get the thermodynamic properties in equilibrium state.

4) **Grand Canonical Ensemble (μVT)**

The system is open when it can exchange both energy and particles with its surrounding. In this context, we name surrounding as reservoir that is in contact with the system of interest. In a general picture, both reservoir and system can be described in NVE ensemble since together they are isolated and the number of particles is constant. However to study the system alone, one should seek thermodynamic variables that are constant during the simulation. For an open system that is in equilibrium with a reservoir, the chemical potential μ, volume V and temperature T are the constant thermodynamic variables. Thus, grand canonical ensemble (μVT) can be used as a statistical description of such systems. The relevant potential for this ensemble is the grand potential defined as follows.

$$\Omega = F - \mu N = U - TS - \mu N \tag{2.6}$$

where F is the Helmholtz free energy of the system. Chemical potential can be defined as the derivative of F with respect to N. So by particle insertion/deletion within the system one could maintain the chemical potential at a particular value. However, care should be taken to ensure that there is no artificial effect on the dynamics of the system. In molecular simulations, Monte Carlo techniques are popular for performing grand canonical ensemble. However, to some extent MD can also simulate constant μVT ensemble [29, 30]. More details on the grand potential will be given in chapter 4.

2.1.2 Interatomic potentials

The true potential energy surface is N-body in nature. It couples the motion of all atoms in the system. We can assume that the non-bonded part of the potential can be written in the following form:

$$V = \sum_i V_{\text{ext}}(\mathbf{r}_i) + \sum_i \sum_{j>i} V^{(2)}(\mathbf{r}_i, \mathbf{r}_j) + \sum_i \sum_{j>i} \sum_{k>j>i} V^{(3)}(\mathbf{r}_i, \mathbf{r}_j, \mathbf{r}_k) + \cdots \tag{2.7}$$

where V_{ext} is the potential energy due to external fields and the remaining terms are the intermolecular interactions where $V^{(2)}$ is the two-body potential that is pair-additive, $V^{(3)}$ is the three-body potential and so on. Three-body and higher-order potentials are computationally expensive and usually are truncated in Eq. 2.7. The non-bonded interactions $V^{(2)}$ contain repulsion, dispersion and a Coulomb term. The bonded interactions include covalent bond-stretching (V_b), angle bending (V_a), improper (V_{id}) and proper dihedrals (V_d).

- **London-van der Waals (vdW) interaction**

In this work, we will consider only Lennard-Jones (LJ) potential to model vdW interaction between two atoms. This is the standard model used in MD and its formula is given by

$$u_{\text{LJ}}(r_{ij}) = 4\epsilon_{ij}\left[\left(\frac{\sigma_{ij}}{r_{ij}}\right)^{12} - \left(\frac{\sigma_{ij}}{r_{ij}}\right)^{6}\right], \tag{2.8}$$

where r_{ij} is the distance between particles i and j, σ is the length scale where the inter-particle potential is zero and ϵ is the depth of the potential well. An alternative form of Eq. 2.8 is

$$u_{\text{LJ}}(r_{ij}) = \frac{C_{ij}^{(12)}}{r_{ij}^{12}} - \frac{C_{ij}^{(6)}}{r_{ij}^{6}}, \tag{2.9}$$

with coefficients $C_{ij}^{(12)}$ and $C_{ij}^{(6)}$ are, respectively, given as

$$C_{ij}^{(12)} = 4\epsilon_{ij}\sigma_{ij}^{12}, \tag{2.10a}$$

$$C_{ij}^{(6)} = 4\epsilon_{ij}\sigma_{ij}^{6}. \tag{2.10b}$$

The r^{-12} term in Eq. 2.8 is the repulsion term that describes at short ranges ($r < \sigma$) two atoms repel each other due to the overlapping electron orbitals. The functional form of the repulsive term has no theoretical justification. It has been shown that, as long as the functional form is repulsive enough the shape of it does not affect the structural properties [31]. On the other hand, r^{-6} has a clear physical justification. This term represents long-rang attraction that rises from dipole-induced-dipole interaction. Not considering the special case of hard spheres, phase transition is impossible without attractive forces.

- **Bonded interactions**

In bonded interactions covalent bond interaction potential V_b represents vibrational frequencies and bond stretching along the chemical bond. It is modeled as a harmonic oscillator with

$$V_b(r_{ij}) = \frac{1}{2}k_{ij}^{(b)}\left(r_{ij} - r_{ij}^{(0)}\right)^2, \tag{2.11}$$

where $k^{(b)}$ is the bond spring constant and $r^{(0)}$ is the equilibrium bond length. Similarly, the bond-angle vibration is defined between triplets of atoms (ijk).

$$V_a(\theta_{ijk}) = \frac{1}{2}k_{ijk}^{(a)}\left(\theta_{ijk} - \theta_{ijk}^{(0)}\right)^2 \tag{2.12}$$

where $k^{(a)}$ is the angular spring constant and $\theta^{(0)}$ is the equilibrium angle between two adjacent bonds. Finally, the potential due to the dihedral interaction is associated with the conformations in the molecule due to the planar orientation of the atoms. Full details on modeling such potentials is given in [21].

- **Electrostatic (Coulomb) interaction**

For a system containing charged atoms, electrostatic forces become important. The net electrostatic potential between two atoms of charges q_i and q_j can be calculated based on Coulombs law:

$$V_c(r_{ij}) = \frac{q_i q_j}{4\pi\epsilon_0\epsilon_r r_{ij}} \tag{2.13}$$

where ϵ_0 is the permittivity of space and ϵ_r is the relative dielectric constant of the medium in which the charges are placed. Unlike LJ potential, Coulomb potential is extremely long-range and requires efficient algorithms to implement it in molecular dynamic simulations. Among these algorithms, Particle Mesh Ewald (PME) [11] and Fast Multiple Method (FMM) are widely used in MD simulations. More detail on these methods can be found in [20].

2.2 Single component LJ fluid in a slit-like nanopore

In this work first we simulate two different confined LJ fluid systems, namely, methane-graphene and argon-graphene slit-channel systems. In both the systems, the LJ fluid is confined between two flat graphene walls in equilibrium with the bulk reservoir. The thermodynamic state of the confined fluid is defined by the bulk reservoir temperature, T, and density, ρ_{b}. We consider supercritical states of the methane and argon fluids given in Table 2.1.

Table 2.1: Thermodynamic states of methane and argon.

	T (K)	ρ_{b} (nm^{-3})
Methane	296	18
Argon	300	24

We perform the equilibrium MD simulations for various channel widths from 2σ to 20σ, where σ is the length-scale parameter for the LJ interaction between fluid molecules (see Table 2.1). To perform the reference MD simulations, we use the similar procedure and the interaction parameters given in Ref. [32]. The MD simulations are performed in the NVT (canonical) ensemble by GROMACS [21]. Methane, argon, and graphene carbon atoms are modeled as LJ type spherical particles. Spherical cutoff of 1.38 nm is used for the Lennard-Jones interactions. The LJ interaction parameters used in MD simulations for various pairs of methane, argon, and graphene carbon particles are given in Table 2.2.

Table 2.2: LJ interaction parameters for methane (CH4), argon (Ar), and graphene carbon (C) atom pairs.

	C_{12} (kJ/mol)	C_6 (kJ/mol)	σ (nm)
CH4-CH4	0.46341E-04	0.15102E-01	0.3812
CH4-C	0.10353E-04	0.47088E-02	0.3606
Ar-Ar	0.96929E-05	0.62194E-02	0.3405
Ar-C	0.46428E-05	0.29922E-02	0.3402

In Table 2.2, for all unlike interactions Lorentz-Berthelot combining rules are applied [33]:

$$\sigma_{ij} = \frac{\sigma_{ii} + \sigma_{jj}}{2} \tag{2.14a}$$

$$\epsilon_{ij} = \sqrt{\epsilon_{ii}\epsilon_{jj}} \tag{2.14b}$$

As shown in Fig. 2.1, two graphene layers are placed along the x-y plane, and the lateral dimensions of the layers are: $L_x = 3.83400$ nm and $L_y = 3.68927$ nm. The separation distance between the two graphene layers, i.e., the channel width, is varied from 2σ to 20σ. Spherical cutoff of 1.38 nm is used for the Lennard-Jones interactions. Wall atoms are kept fixed at their original positions.

Periodic boundary conditions are specified in the x, y, and z directions. The simulation box is padded with a vacuum layer of 60σ width in the z dimension to avoid the interactions between periodic images in the z dimension. Temperature is maintained using the Nosé-Hoover thermostat [23] with 0.5 ps time constant. All systems are equilibrated for 2 ns and production runs of 8 ns are performed with 1 fs time step. The density profiles are computed using 0.05σ bin size along the z direction.

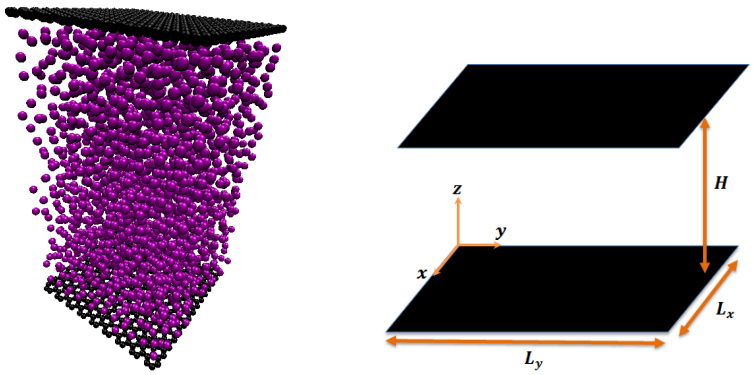

(a) (b)

Figure 2.1: (a) Simulation setup for a single component LJ fluid confined between two graphene sheets. (b) Schematic view of the graphene slit nanochannel.

2.3 Lennard-Jones binary mixtures in a slit-like nanopore

In this section, we consider binary LJ mixtures of methane and hydrogen inside a slit-like nano confinement. The thermodynamic state of the confined mixture is specified based on the bulk mixture reservoir that is in equilibrium with the nanopore.

As shown in Fig. 2.2, the mixture of methane and hydrogen is simulated in graphene nanopores. The slit pores considered in this study consist of two graphene layers separated in z-direction. The lateral dimensions of the layers in the x-y plane are $3.834\times3.689\ nm^2$ and separation distance, H, between the two sheets is varied from 0.762 nm ($= 2\sigma_{22}$ where σ_{22} is the length-scale parameter for LJ interaction between methane molecules) to 6.34 nm. In this study, Visual Molecular Dynamics (VMD) [34] is used to construct the geometries.

In this study, the slit channels are in equilibrium with two bulk mixture compositions: Methane-rich ($x_m = 0.7$) and hydrogen-rich bulk mixture ($x_m = 0.3$) with total bulk density of 17.73 atoms/nm^3. Methane and hydrogen molecules are modeled as single-site LJ spherical particles with interaction parameters given in Table 2.3. The parameters are taken from [35] and like the single com-

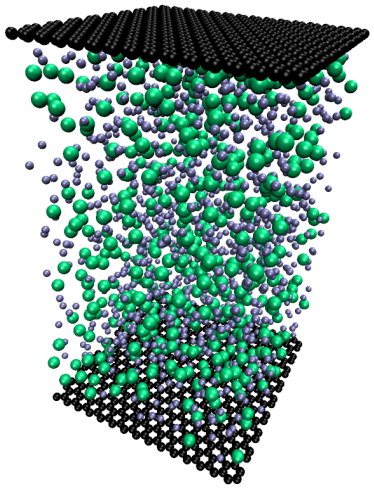

Figure 2.2: Simulation setup for the mixture of methane and hydrogen molecules confined between two graphene sheets.

ponent case in Section 2.2, for all unlike interactions we use Lorentz-Berthelot combining rules (Eq. 2.14).

Table 2.3: LJ interaction parameters for methane (CH4), Hydrogen (H2), and graphene carbon (C) atom pairs.

	σ (nm)	ϵ (kJ/mol)
C-C	0.340	0.2328
H2-H2	0.2915	0.3159
CH4-CH4	0.3812	1.2314

In Fig. 2.2, wall atoms are kept fixed throughout the simulation. Thus, the bonded interactions of the graphene carbon atoms are excluded. The spherical cut-off used for Lennard-Jones interactions is 1.7 nm. Periodic boundary conditions are applied in all directions with an extra vacuum of 10 nm in z-direction. Since no electrostatic forces are involved in the system, the extra vacuum space only needs to be larger than LJ cut-off used in the simulation. This gap ensures that the system is not interacting with its mirror image in the z-direction. MD simulations for confined methane-hydrogen mixture are performed in GROMACS molecular package [21]. To maintain the temperature at 300 K, NoséHoover thermostat is used with time constant of 0.2 pico seconds. All systems are equilibrated for 5ns in the NVT (canonical) ensemble. Following equilibration, production run for 45ns performed with 1 femto second time step. The numbers of hydrogen and methane molecules required in nanopores are obtained based on a theoretical approach that is discussed in detail in Chapter 3.

In this study, for mixtures the focus is on the structure of the fluids in the confinement. By minimizing the grand potential of the confined fluid, we will show in Chapter 4 that fluid densities can be related to the potential of the mean force (PMF) profiles. Therefore, in our simulations in addition to positions, force components are also dumped with interval of 0.5 pico seconds. Processing the trajectories, density profiles are computed using bin size of $0.05\sigma_{22}$ along z direction.

CHAPTER 3

INTERATOMIC POTENTIAL-BASED MULTISCALE THEORY

3.1 Empirical Potential-Based Quasi-Continuum Theory (EQT)

An empirical potential-based quasi-continuum theory (EQT) is a multiscale approach that provides a framework to seamlessly integrate atomistic details into a continuum-based model. Over the past few years, EQT has been developed and studied to predict structure and potential profiles of single component Lennard-Jones fluids [36, 32], carbon dioxide [37] and water [38, 39] in nano slit-like channels. In this chapter, we present a modified version of EQT that is general, more accurate and applicable to mixtures. Moreover, we will show in Chapter 4 that EQT potentials can also be used to construct the excess free energy functional ($F^{ex}[\rho(r)]$) required in the classical density functional theory (cDFT).

As shown in Fig. 2.1b, for a fluid confined in a slit-like geometry, it is reasonable to assume that the fluid concentration in the channel has a one-dimensional variation along the z direction. The objective is to determine the fluid density, ρ, and the total potential profile, U, as a function of z inside the channel. For this purpose, in order to relate the density and the total potential, one can use the 1-D steady-state Nernst-Planck (NP) equation,

$$\frac{d}{dz}\left(\frac{d\rho}{dz}+\frac{\rho}{RT}\frac{dU}{dz}\right)=0 \tag{3.1}$$

with boundary conditions

$$\rho(0)=\rho(H)=0 \tag{3.2a}$$

$$\frac{1}{H}\int_0^H \rho(z)dz=\rho_{avg} \tag{3.2b}$$

In Eqs. 3.1 and 3.2, T is the fluid temperature, R is the ideal gas constant, H is the channel width, ρ_{avg} is the average density of the confined fluid and the total potential, $U(z)$, is the sum of fluid-fluid and wall-fluid contributions, i.e,

$$U(z)=U^{\mathrm{ff}}(z)+U^{\mathrm{wf}}(z). \tag{3.3}$$

One needs to solve for both $U(z)$ and $\rho(z)$. This requires an additional equation.

The main idea of EQT is to express U in terms of ρ by using empirical pair potentials and continuum representation of the wall and fluid atoms. Once the expressions for the fluid-fluid (U^{ff}) and the wall-fluid (U^{wf}) potentials are obtained, Eq. 3.1 is solved self-consistently with the boundary conditions specified in Eq. 3.2 to determine the density and potential profile of the confined fluid.

3.2 EQT for single component fluids

In this section, we introduce the EQT formalism for the single component fluid in the presence of an external potential. Although the case study we consider is the fluid inside a slit-like confinement, the EQT formalism presented here is general and applicable for 3D geometries as well. As mentioned in Section 3.1, in the EQT, the total potential, $U(\mathbf{r})$, at a given location $\mathbf{r}$ can be computed as a sum of wall-fluid and fluid-fluid interactions. For the rest of this chapter, we are going to explain how the wall-fluid and the fluid-fluid potentials can be expressed as a function of the concentrations and inter-atomic force field of the wall and fluid atoms.

3.2.1 Wall-fluid potential

From atomistic perspective, the wall-fluid potential at a given location $\mathbf{r}$ is given by:

$$U^{\text{wf}}(\mathbf{r}) = \sum_{i=1}^{N_w} u^{\text{wf}}(|\mathbf{r} - \mathbf{r}_i|), \tag{3.4}$$

where the summation goes over all the number of wall atoms N_w, which are interacting through wall-fluid potential, u^{wf}, and $\mathbf{r}_i$ is the location of the wall atom i. As shown in Fig. 3.1, in the EQT we represent wall atoms as a continuum medium with a density of $\rho_w(\mathbf{r}_i)$. Thus, Eq. 3.4 can be rewritten as,

$$U^{\text{wf}}(\mathbf{r}) = \sum_{i=1}^{N_{lw}} u^{\text{wf}}(|\mathbf{r} - \mathbf{r}_i|)\rho_w(\mathbf{r}_i)\Delta V_i, \tag{3.5}$$

where the summation goes over the number of radial wall layers denoted by N_{lw}, that represents wall atoms within the sphere of radius R^{wf}_{cut}. In Eq. 3.5, ΔV_i is the volume of the i^{th} radial layer and $\rho_w(\mathbf{r}_i)$ represents the density of wall atoms in the i^{th} radial layer. Assuming that the wall atoms are kept fixed at their locations (i.e. rigid wall), the continuum approximation for the discrete summation in the Eq. 3.5 is given by:

$$U^{\text{wf}}(\mathbf{r}) = \int \rho_w(\mathbf{r}')u^{\text{wf}}(|\mathbf{r} - \mathbf{r}'|)d\mathbf{r}', \tag{3.6}$$

where $d\mathbf{r}'$ is an infinitesimal volume element in the wall structure, $\rho_w(\mathbf{r}')$ is the wall density at location $\mathbf{r}'$ and $u^{\mathrm{wf}}(|\mathbf{r}-\mathbf{r}'|)$ is the wall-fluid potential between the two points $\mathbf{r}$ and $\mathbf{r}'$. For a more detailed implementation of the EQT wall-fluid potential inside a slit-like channel, see Ref. [36].

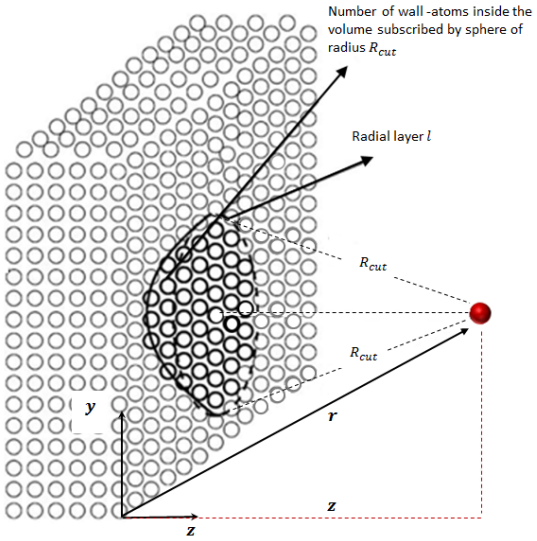

Figure 3.1: The shaded region in the figure is the volume circumscribed by the sphere of radius R_{cut} located at the point $\mathbf{r}$ (the red circle).

3.2.2 Fluid-fluid potential

In contrast with the wall-fluid potential, the fluid-fluid interactions are not trivial and require special considerations due to fluid-fluid correlations. In order to obtain a continuum expression for the fluid-fluid potential, we need to have a good understanding of the correlations in the fluid medium due to the interaction between the fluid atoms. Recall that for the wall-fluid potential, because of the rigid wall assumption , we did not take into account the effect of fluid atoms on the wall structure. However, for the fluid-fluid potential this is not the case. Hence, in this section, before introducing the EQT formulation for the fluid-fluid potential, we will provide necessarily information about particle densities and distribution functions.

Particle densities

In general, n-particle density, $\rho^{(n)}(\mathbf{r}^n)$, is the probability density of finding n particles of the system with coordinates $\mathbf{r}^n \equiv \mathbf{r}_1, \mathbf{r}_2, ..., \mathbf{r}_n$. Thus, $\rho^{(n)}(\mathbf{r}^n)d\mathbf{r}^n$ is the probability of finding n particles in the volume elements $d\mathbf{r}^n \equiv d\mathbf{r}_1, d\mathbf{r}_2, ..., d\mathbf{r}_n$ irrespective of the positions of the remaining particles and irrespective of all momenta. Thus, $\rho^{(1)}(\mathbf{r})d\mathbf{r}$, with $\rho^{(1)}(\mathbf{r})$ as the 1-particle density, is the probability

of finding a single particle in a volume element $d\mathbf{r}$ at a location $\mathbf{r}$ irrespective of the positions of the remaining particles. Therefore,

$$\int \rho^{(1)}(\mathbf{r})d\mathbf{r} = N, \tag{3.7}$$

where, N is the total number of particles in the system. For a uniform bulk fluid, 1-particle density is equal to the overall number density:

$$\rho^{(1)}(\mathbf{r}) = \frac{N}{V} = \rho_b, \tag{3.8}$$

where, V is the volume of the system and ρ_b is the bulk density of the uniform system.

The n-particle density can also be considered as a joint probability density of finding n particles at $\mathbf{r}_1, \mathbf{r}_2, ..., \mathbf{r}_n$ simultaneously. For example, $\rho^{(2)}(\mathbf{r}_1, \mathbf{r}_2)d\mathbf{r}_1 d\mathbf{r}_2$ is the joint probability of finding two particles located at $\mathbf{r}_1$ and $\mathbf{r}_2$ at the same time.

Distribution functions

The particle distribution functions measure the extent of which the structure of a fluid deviates from complete randomness. The n-particle distribution function $g^{(n)}(\mathbf{r}^n)$ is defined in terms of the corresponding particle densities as

$$g^{(n)}(\mathbf{r}^n) = \frac{\rho^{(n)}\left(\mathbf{r}_1, \mathbf{r}_2, ..., \mathbf{r}_n\right)}{\prod_{i=1}^{n} \rho^{(1)}(\mathbf{r}_i)}, \tag{3.9}$$

where $\rho^{(n)}\left(\mathbf{r}_1, \mathbf{r}_2, ..., \mathbf{r}_n\right)$ is the joint probability when the particles interact and $\prod_{i=1}^{n} \rho^{(1)}(\mathbf{r}_i)$ is the joint probability when particles do not interact, i.e., complete randomness.

Therefore, from Eq. 3.9 the 2-particle distribution function, $g^{(2)}(\mathbf{r}_1, \mathbf{r}_2)$, i.e., pair distribution function, is given by

$$g^{(2)}(\mathbf{r}_1, \mathbf{r}_2) = \frac{\rho^{(2)}\left(\mathbf{r}_1, \mathbf{r}_2\right)}{\rho^{(1)}(\mathbf{r}_1)\rho^{(1)}(\mathbf{r}_2)}, \tag{3.10}$$

i.e.,

$$\rho^{(2)}\left(\mathbf{r}_1, \mathbf{r}_2\right) = g^{(2)}(\mathbf{r}_1, \mathbf{r}_2)\rho^{(1)}(\mathbf{r}_1)\rho^{(1)}(\mathbf{r}_2). \tag{3.11}$$

Estimating number of neighbors using pair distribution function

In probability theory, a conditional probability measures the probability of an event given that another event has occurred. In other words, given the two events A and B the conditional probability is defined as

$$P(A|B) = \frac{P(A \cap B)}{P(B)}. \tag{3.12}$$

We can use Eq. 3.12 to determine the number of fluid particles at the location $\mathbf{r}_i$ around a particle located at $\mathbf{r}$. To do so, we define events A and B to represent particles located at the positions $\mathbf{r}_i$ and $\mathbf{r}$, respectively. Thus Eq. 3.12 can be written as

$$\rho(\mathbf{r}_i|\mathbf{r})d\mathbf{r}_i = \frac{\rho^{(2)}(\mathbf{r}_i,\mathbf{r})d\mathbf{r}d\mathbf{r}_i}{\rho^{(1)}(\mathbf{r})d\mathbf{r}}, \tag{3.13}$$

where, $\rho(\mathbf{r}_i|\mathbf{r})$ is the probability density of having a particle at the position $\mathbf{r}_i$ given a particle at the position $\mathbf{r}$. Simplifying Eq. 3.13 yields,

$$N(\mathbf{r}_i|\mathbf{r}) = \frac{\rho^{(2)}(\mathbf{r}_i,\mathbf{r})}{\rho^{(1)}(\mathbf{r})}d\mathbf{r}_i, \tag{3.14}$$

where, $N(\mathbf{r}_i|\mathbf{r})$ is the number of particles at the position $\mathbf{r}_i$ in a volume element $d\mathbf{r}_i$ relative to a particle located at $\mathbf{r}$. Using Eq. 3.11, Eq. 3.14 can be re-written in terms of the pair distribution function,

$$N(\mathbf{r}_i|\mathbf{r}) = \rho^{(1)}(\mathbf{r}_i)g^{(2)}(\mathbf{r}_i,\mathbf{r})d\mathbf{r}_i. \tag{3.15}$$

Using Eqs. 3.13 and 3.15, we can redefine the pair distribution as,

$$g^{(2)}(\mathbf{r}_i,\mathbf{r}) = \frac{\rho(\mathbf{r}_i|\mathbf{r})}{\rho^{(1)}(\mathbf{r})}. \tag{3.16}$$

In other words, one can think of the pair distribution function as a criterion to which a tagged particle will affect its surrounding.

Fluid-fluid potential formulation

Similar to the wall-fluid potential, in a particle-based framework like MD, the fluid-fluid potential, $U^{\text{ff}}(\mathbf{r})$, of a fluid molecule located at $\mathbf{r}$ can be computed as a sum of interactions with all the neighbor fluid atoms, as

$$U^{\text{ff}}(\mathbf{r}) = \sum_{i=1}^{N_f} u^{ff}\left(|\mathbf{r}_i - \mathbf{r}|\right), \tag{3.17}$$

where u^{ff} is the fluid-fluid pair potential and N_f is the total number of fluid neighbors within a cut-off radius $R^{\text{ff}}_{\text{cut}}$. As shown in Fig. 3.2, in a continuum framework of EQT, in order to calculate the fluid-fluid potential of a molecule at a specific location, we need to take into account its effect on its neighboring fluid molecules. In other words, due to the existing inter-atomic potential between the fluid molecules, the density of the fluid around a tagged particle is different than the bulk. Thus, in a continuum framework of EQT, Eq. 3.17 is represented as,

$$U^{\text{ff}}(\mathbf{r}) = \sum_{i=1}^{N_{lf}} u^{\text{ff}}\left(|\mathbf{r}_i - \mathbf{r}|\right)\rho(\mathbf{r}_i|\mathbf{r})\Delta\Omega_i, \tag{3.18}$$

where N_{lf} is the total number of discrete volumes within a cut-off sphere from the point $\mathbf{r}$ and $\Delta\Omega_i$ is the volume of the i^{th} discrete layer. Using the definition of the pair distribution function given by Eq. 3.16, Eq. 3.18 can be reformulated in terms of the pair distribution function and $\rho(\mathbf{r}_i)$, which is equivalent to the 1-particle density, $\rho^{(1)}(\mathbf{r}_i)$,

$$U^{\mathrm{ff}}(\mathbf{r}) = \sum_{i=1}^{N_{lf}} u^{\mathrm{ff}}\left(|\mathbf{r}_i - \mathbf{r}|\right) g^{(2)}(\mathbf{r}_i, \mathbf{r}) \rho(\mathbf{r}_i) \Delta\Omega_i. \tag{3.19}$$

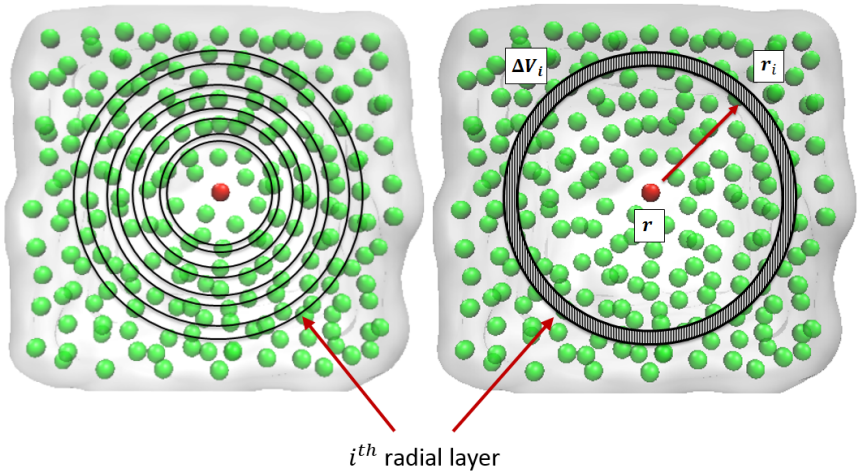

Figure 3.2: Plot of discrete fluid volumes that are distributed radially around the tagged particle (red circle) located at $\mathbf{r}$.

A continuum approximation for the discrete summation in Eq. 3.19 is

$$U^{\mathrm{ff}}(\mathbf{r}) = \int u^{\mathrm{ff}}\left(|\mathbf{r} - \mathbf{r}'|\right) g^{(2)}\left(\mathbf{r}, \mathbf{r}'\right) \rho\left(\mathbf{r}'\right) d\mathbf{r}', \tag{3.20}$$

where $d\mathbf{r}'$ is an infinitesimal fluid volume element, $\rho(\mathbf{r}')$ is the average fluid density at location $\mathbf{r}'$, and $u^{\mathrm{ff}}(|\mathbf{r} - \mathbf{r}'|)$ is the effective fluid-fluid pair potential between the two points $\mathbf{r}$ and $\mathbf{r}'$. For a more detailed implementation of the EQT fluid-fluid potential inside a slit-like channel, see Refs. [36, 38].

I. EQT effective fluid-fluid pair potential

The main idea in the EQT is to use the effective interactions from a more detailed high resolution level. For example, if the system under study consists of only Lennard-Jones type of atoms/molecules, the effective fluid-fluid (u^{ff}) and wall-fluid (u^{wf}) pair potentials are the standard 12-6 Lennard-Jones potentials.

$$u^{\mathrm{wf}}(r) = 4\epsilon_{\mathrm{wf}}\left[\left(\frac{\sigma_{\mathrm{wf}}}{r}\right)^{12} - \left(\frac{\sigma_{\mathrm{wf}}}{r}\right)^{6}\right], \tag{3.21a}$$

$$u^{\mathrm{ff}}(r) = 4\epsilon_{\mathrm{ff}}\left[\left(\frac{\sigma_{\mathrm{ff}}}{r}\right)^{12} - \left(\frac{\sigma_{\mathrm{ff}}}{r}\right)^{6}\right], \tag{3.21b}$$

where $\sigma_{\rm wf}$, $\epsilon_{\rm wf}$, $\sigma_{\rm ff}$, and $\epsilon_{\rm ff}$ are the usual LJ parameters for the wall-fluid and fluid-fluid interactions. For the complex systems such as carbon dioxide, water, etc, aside from the van der Waals interactions, care should be taken regarding the electrostatic forces. As of now, in the EQT frame work, we treat molecules as single-site LJ particles. Thus, for any complex systems such as mentioned above, we need to properly coarse-grain the degrees of freedom and incorporate their effect into an optimal pair potential to use in the EQT formulation. For this purpose, we coarse-grain degrees of freedom from the detailed all-atom level to the particle-based CG level, and to the continuum-based level. This procedure is shown for water molecules confined inside a slit-like channel (see Fig. 3.3).

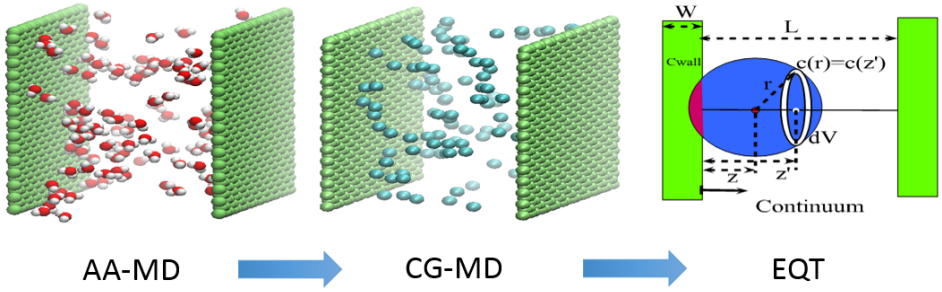

Figure 3.3: Systematic coarse-graining procedure form all-atom level to the cheaper particle-based CG level and to continuum-based level.

In this system, the wall-fluid and fluid-fluid interactions are coarse-grained by the relative entropy method [40]. The CG potentials are optimized such that they reproduce accurate density distribution of water molecules inside the channel. Further information on the EQT for confined water can be found in reference [38].

II. Approximations for pair distribution function

There exist several approximations for the pair distribution function. Among them, mean field theory (MFT) has been widely used, especially in the cDFT literature to treat long-range attractions in the excess part of the intrinsic Helmholtz free energy [41, 42, 43, 44]. MFT assumes that there is no correlation between the fluid molecules (i.e., $g^{(2)}(\mathbf{r},\mathbf{r}') = 1$). Although MFT is computationally convenient and easy to grasp, it can be quantitatively problematic and even sometimes qualitatively incorrect [45]. In addition, since the pair potential is highly repulsive as $r \longrightarrow 0$, the mean field approximation will cause numerical singularities. To avoid this problem and to introduce a better approximation for the pair correlation, we follow an approach similar to Tang and Wu's work [45]. We approximate the pair distribution function by

$$g^{(2)}(\mathbf{r},\mathbf{r}') \approx g^{hs}(|\mathbf{r}-\mathbf{r}'|), \tag{3.22}$$

where g^{hs} is the radial distribution function (RDF) of homogeneous hard spheres at bulk density, ρ_b. Hard sphere particles are defined as impenetrable spheres that cannot overlap. They usually serve as a model to study the extremely strong repulsion between the atoms/molecules at very close distances. For instance, modeling a dense Lennard-Jones fluid system with a group of hard sphere particles is not a bad approximation. As represented by Fig. 3.4, hard spheres interact via an infinite potential at their contact and zero elsewhere, i.e,

$$u^{\text{hs}} = \begin{cases} \infty & \text{for} \quad r < d \\ 0 & \text{for} \quad r > d \end{cases} \tag{3.23}$$

where d is the hard sphere diameter.

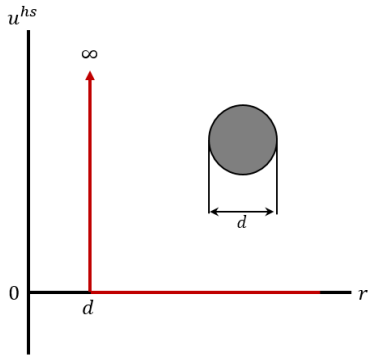

Figure 3.4: Plot of the hard sphere potential of diameter d.

Although there is no attraction between the hard spheres, they still arrange in layers from a tagged particle. Basically, geometry, density and the strong repulsion make the system of bulk hard spheres to acquire a radial distribution function ($g^{\text{hs}}(r)$). An example of hard sphere RDF is given in Fig. 3.5.

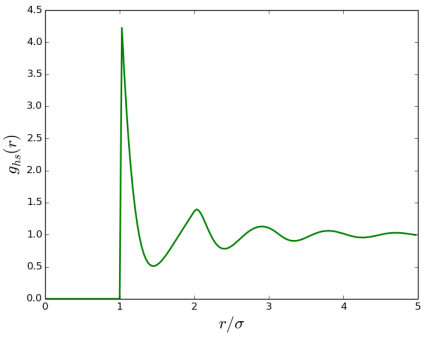

Figure 3.5: Bulk hard sphere radial distribution function of $\eta \approx 0.5$.

To fully determine the hard sphere RDF, we need to know the packing fraction $\eta = \pi\rho_b d^3/6$. In order to mimic a real LJ fluid in which the particles interact with a soft-core, the hard sphere diameter is calculated based on the relation

proposed by Barker and Henderson [46],

$$d(T) = \int_0^{\sigma} \left(1 - \exp\left[-\frac{u^{\text{ff}}(r)}{k_B T}\right]\right) dr \tag{3.24}$$

where σ is the length-scale parameter for LJ interaction and k_B is the Boltzmann constant. In fact, Eq. 3.24 is obtained based on minimization of the free energy difference between a real LJ bulk fluid system and the corresponding hard sphere system with the diameter d. Once the diameter is determined, the RDF is obtained using existing analytical expressions based on Percus-Yevick approximation [47, 48, 49]. A complete review on different closures and approximations can be found elsewhere [50].

III. Correlation-correction potential

Since, the hard sphere RDF approximation may not accurately reproduce the properties of a real fluid, we introduce an isotropic correlation-correction potential denoted as , $u^{\text{ff}}_{\text{ccp}}(r)$, and reformulate Eq. 3.20 as

$$U^{\text{ff}}(\mathbf{r}) = \int \rho(\mathbf{r}') \left(u^{\text{ff}}(|\mathbf{r} - \mathbf{r}'|) g^{\text{hs}}(|\mathbf{r} - \mathbf{r}'|) + u^{\text{ff}}_{\text{ccp}}(|\mathbf{r} - \mathbf{r}'|)\right) d\mathbf{r}'. \tag{3.25}$$

To model the correlation-correction function we use uniform cubic B-splines as

$$u^{\text{ff}}_{\text{ccp}}(r) = \begin{bmatrix} 1 & t & t^2 & t^3 \end{bmatrix} \frac{1}{6} \begin{bmatrix} 1 & 4 & 1 & 0 \\ -3 & 0 & 3 & 0 \\ 3 & -6 & 3 & 0 \\ -1 & 3 & -3 & 1 \end{bmatrix} \begin{bmatrix} c_j \\ c_{j+1} \\ c_{j+2} \\ c_{j+3} \end{bmatrix}, \tag{3.26}$$

where r is the separation distance between any two fluid molecules with the cut-off radius denoted by R_{cut}. The separation distance is discretized into $n-1$ intervals of equal size $\Delta r = R_{\text{cut}}/(n-1)$ such that $r_i = i \times \Delta r$, where $i \in (0...n-1)$. In Eq. 3.26, the $n+2$ values $\{c_j\}$ are called spline knots where index j is determined such that $r_j \leq r < r_{j+1}$, and t is given by

$$t = \frac{r - r_j}{\Delta r}. \tag{3.27}$$

In Fig. 3.6, a schematic picture of the correlation-correction potential is shown.

3.2.3 Optimization

In this section, we introduce a metric called PMF-matching proposed by [39] in order to optimize the spline knot values used to model the correlation-correction function. For a slit-like channel, where the fluid inhomogeneity is in one direction (z), as a solution to Eq. 3.1, the equilibrium density distribution must

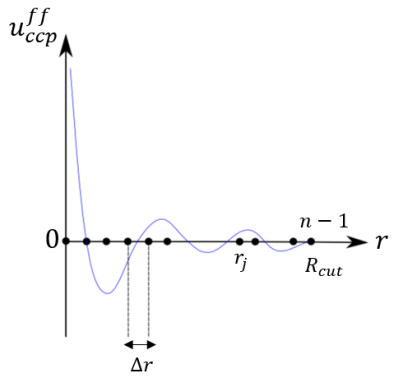

Figure 3.6: A schematic plot of the fluid-fluid correlation correction potential.

satisfy the Boltzmann relation given by

$$\rho(z) = \rho_0 \exp\left(-\frac{\tilde{U}(z)}{k_{\mathrm{B}}T}\right), \tag{3.28}$$

where ρ_0 is the density at the reference point z_0 and $\tilde{U}(z)$ is the total potential of mean force (PMF) relative to the reference point z_0.

$$\tilde{U}(z) = U^{\mathrm{ff}}(z) + U^{\mathrm{wf}}(z) - U(z_0). \tag{3.29}$$

In the PMF matching technique, the mean-square error in density is minimized such that it reproduces the target potential of mean force within the specified tolerance. In the PMF matching, for a slit-like system, the metric is defined as

$$\epsilon_B = \frac{1}{2H}\int_0^H \left(\rho_0^{tgt} \exp\left(-\frac{\tilde{U}(z)}{k_{\mathrm{B}}T}\right) - \rho^{tgt}(z)\right)^2 dz, \tag{3.30}$$

where ρ^{tgt} is the target density obtained from the reference all-atom MD simulations. To obtain the optimal knot values in correction-correlation function, Eq. 3.30 is minimized using the Newton-Raphson optimization technique. For further information on the details of optimization for a slit-like channel, see Ref. [39].

3.3 EQT formalism for mixtures

In order to extend EQT frame work for multi-component fluid system inside the slit-channel, we need to solve Nernst-Planck equation for each species present in the mixture, i.e,

$$\frac{d}{dz}\left(\frac{d\rho_\alpha}{dz} + \frac{\rho_\alpha}{RT}\frac{dU_\alpha}{dz}\right) = 0 \tag{3.31}$$

with boundary conditions

$$\rho_\alpha(0) = \rho_\alpha(H) = 0 \tag{3.32a}$$

$$\frac{1}{H}\int_0^H \rho(z)_\alpha dz = \rho_{\alpha,avg} \tag{3.32b}$$

where $\alpha = 1, 2, \cdots, m$ is the label of a fluid component and m is the number of fluid components in the mixture. As mentioned in Section 3.1, we need to formulate total potential in terms of the fluid density, in order to be able to self-consistently solve the equations mentioned above.

In general, the total potential of a fluid component α, $U_\alpha(\mathbf{r})$, at a given location $\mathbf{r}$ can be computed as a sum of wall-fluid and fluid-fluid interactions:

$$U_\alpha(\mathbf{r}) = U_\alpha^{\mathrm{wf}}(\mathbf{r}) + U_\alpha^{\mathrm{ff}}(\mathbf{r}) \tag{3.33}$$

where U_α^{wf} and U_α^{ff} are the wall-fluid and fluid-fluid potential of component α, respectively.

Similar to what we did for single component case in Section 3.2, the wall structure is locally represented by a single density distribution, $\rho_w(\mathbf{r})$. Therefore, for the mixtures, Eq. 3.6 holds for each fluid component.

$$U^{\mathrm{wf}}(\mathbf{r}) = \int \rho_w(\mathbf{r}')u_\alpha^{\mathrm{wf}}(|\mathbf{r}-\mathbf{r}'|)d\mathbf{r}', \tag{3.34}$$

where u_α^{wf} is the wall-fluid pair potential for component α.

Similarly, Eq. 3.20 can be generalized to account for multi-component fluid system in EQT. Thus, for a mixture of fluids, the fluid-fluid potential energy can be expressed as

$$U_\alpha^{\mathrm{ff}}(\mathbf{r}) = \sum_{\beta=1}^{m}\int \rho_\beta(\mathbf{r}')\, g_{\alpha\beta}^{(2)}(\mathbf{r},\mathbf{r}')\, u_{\alpha\beta}^{\mathrm{ff}}(|\mathbf{r}-\mathbf{r}'|)\, d\mathbf{r}', \tag{3.35}$$

where $u_{\alpha\beta}^{\mathrm{ff}}$ is the fluid-fluid pair potential between components α and β. Using the bulk hard sphere approximation for the pair distribution function, the EQT fluid-fluid potentials for mixtures is given by

$$U_\alpha^{\mathrm{ff}}(\mathbf{r}) = \sum_{\beta=1}^{m}\int \rho_\beta(\mathbf{r}')\left(g_{\alpha\beta}^{\mathrm{hs}}(\mathbf{r},\mathbf{r}')\, u_{\alpha\beta}^{\mathrm{ff}}(|\mathbf{r}-\mathbf{r}'|) + u_{\mathrm{ccp},\alpha\beta}^{\mathrm{ff}}(|\mathbf{r}-\mathbf{r}'|)\right) d\mathbf{r}' \tag{3.36}$$

As an example, in the binary mixture of hydrogen and methane molecules, the fluid-fluid potential for hydrogen molecule, denoted by $\alpha = 1$, is written as

$$\begin{aligned} U_1^{\mathrm{ff}}(\mathbf{r}) \quad = \quad & \int \rho_1(\mathbf{r}')\left(g_{11}^{\mathrm{hs}}(\mathbf{r},\mathbf{r}')\, u_{11}^{\mathrm{ff}}(|\mathbf{r}-\mathbf{r}'|) + u_{\mathrm{ccp},11}^{\mathrm{ff}}(|\mathbf{r}-\mathbf{r}'|)\right) d\mathbf{r}' + \\ & \int \rho_2(\mathbf{r}')\left(g_{12}^{\mathrm{hs}}(\mathbf{r},\mathbf{r}')\, u_{12}^{\mathrm{ff}}(|\mathbf{r}-\mathbf{r}'|) + u_{\mathrm{ccp},12}^{\mathrm{ff}}(|\mathbf{r}-\mathbf{r}'|)\right) d\mathbf{r}' \end{aligned} \tag{3.37}$$

where interactions 11 and 12 refer to hydrogen-hydrogen and hydrogen-methane interactions, respectively. Since in the hydrogen potential, the hydrogen-methane interaction is weighted by the methane density, we introduce two different correlation-correction potentials to optimize for.

CHAPTER 4

AN EQT-BASED CDFT APPROACH FOR CONFINED FLUIDS

In this chapter, we integrate EQT frame work with classical density functional theory (cDFT), i.e., EQT-cDFT approach, in order to determine thermodynamic properties of confined fluids. The combination of EQT and cDFT provides a simple and fast approach that not only predicts the equilibrium structure, but also other thermodynamic properties, such as the local pressure profile, adsorption, solvation force, surface tension, etc. [51]

The remainder of this chapter is organized as follows. First we will provide some information on different free energies and the ensembles associated with them. We will focus more on the grand potential and obtain the thermodynamic properties based on it. In Section 4.3, we briefly introduce the classical density functional theory. Finally, in Section 4.4 we introduce the EQT-cDFT approach and explain how EQT potentials can be utilized to construct the excess free energy functional required in the cDFT.

4.1 Free energies and different ensembles

According to the first law of thermodynamics, an infinitesimal change in system internal energy , E, can be related to other thermodynamic properties as

$$dE = TdS + \sum_i x_i X_i, \tag{4.1}$$

where S is the entropy, T is the temperature, and X_i are work coordinates. In Eq. 4.1, the variables appear as conjugate pairs (x,X) consisting of intensive and extensive quantities. For example, for a usual fluid system that is allowed to change volume and to exchange particles with its surrounding, Eq. 4.1 reads,

$$dE = TdS - PdV + \mu dN, \tag{4.2}$$

where P is the pressure, V is the system volume, μ is the chemical potential and N is the number of particles in the system. In Eq. 4.2, P and μ are the conjugate variables to $-V$ and N, respectively.

Now consider the same system containing an interface (e.g. a plate), one can change the internal energy by changing the area of the interface. In this case

Eq. 4.1 is written as

$$dE = TdS - PdV + \mu dN + \gamma dA, \tag{4.3}$$

where γ is the interfacial tension which is a conjugate variable to the surface area, A.

As mentioned in Section 2.1.1, for each ensemble, there exist a relevant thermodynamic potential which is minimum when the system is in equilibrium. Thus, knowing the relevant free energy for a system is crucial to obtain the equilibrium thermodynamic properties. Here, we briefly discuss the free energies and elaborate more on the grand potential, namely, Landau free energy.

1. **Helmholtz Free Energy**

The Helmholtz free energy is defined as,

$$F = E - TS. \tag{4.4}$$

Using Eq. 4.2, an infinitesimal change in F is given by

$$dF = -PdV - SdT + \mu dN. \tag{4.5}$$

Thus, in equilibrium, if the set of control variables are N, V and T, the change in the Helmholtz free energy is zero and consequently F is minimum. Hence, for a system that does not exchange particles and has a constant volume, but is allowed to exchange heat with the environment, the relevant thermodynamic quantity is the Helmholtz free energy.

2. **Gibb's Free Energy**

The Gibb's free energy is defined as,

$$G = E - TS + PV. \tag{4.6}$$

Using Eq. 4.2, an infinitesimal change in G is given by

$$dG = VdP - SdT + \mu dN. \tag{4.7}$$

Eq. 4.7 indicates that, if the set of control variables are N, P and T, the change in the Gibb's free energy is zero and consequently G is minimum under these conditions. Hence, for a system of constant number of particles (i.e. no particle exchange), constant pressure and constant temperature (i.e. allowing heat exchange to the environment) the relevant thermodynamic quantity is the Gibb's free energy. The NPT ensemble in molecular dynamic simulation packages is a tool to mimic these conditions in a computer simulation.

3. **Grand potential**

Finally the relevant thermodynamic potential for an open system that is in equilibrium with a bulk phase (i.e., the system can exchange heat and particle with the bulk phase) is the grand potential.

$$\Omega = -PdV - SdT - Nd\mu. \tag{4.8}$$

Using Eq. 4.2, an infinitesimal change in the Ω is given by

$$d\Omega = VdP - SdT + \mu dN. \tag{4.9}$$

Eq. 4.9 suggests that, the relevant condition or ensemble for which the grand potential is minimum in equilibrium is the constant μ , V, and T ensemble. Under these thermodynamic conditions, the system is allowed to exchange particle and heat with the environment, while its volume is maintained. For example, if a fluid confined between two plates is in equilibrium and in contact with the a bulk reservoir, it is necessary that the chemical potential of the reservoir and the confined fluid be the same.

Thus far, we assumed a system with no interface (Eq. 4.8). When a fluid is narrowly confined between to parallel plates of area A, additional control variables comes into play. These new variables are the surface area of the plates, A and the spacing between them , H. Therefore, the generalisation of Eq. 4.9 for a confined fluid inside a slit-like channel is

$$d\Omega = -SdT - PdV - Nd\mu + 2\gamma dA - (f_{\mathrm{S}}A)dH, \tag{4.10}$$

where f_{S} is commonly referred to as the solvation force. In fact, f_{S} has a dimension of pressure, but it is interpreted a force required to hold the plates in place.

4.2 Thermodynamic properties

As mentioned in Section 2.2, we consider a fluid confined in a slit-like channel, which consists of two infinitely long plane parallel walls placed in the x-y plane at $z = 0$ and $z = H$. Therefore, the system is periodic in the x and y directions, and we focus only on the z-variation of the properties. From Eq. 4.10, one can determine various thermodynamic properties of a confined fluid. In this work, we compute the properties such as total adsorption, local pressure tensor, interfacial tension, and solvation force as described below.

The total adsorption is the difference between the average number of fluid molecules in the confined region with and without the channel walls. The total adsorption per unit surface area, Γ, can be computed as an integral over the

confined region:

$$\Gamma(H) = \frac{1}{2}\int_0^H (\rho(z) - \rho_{\mathrm{b}})\, dz, \tag{4.11}$$

where ρ_{b} is the bulk density of the fluid at a given T and μ, and the factor of $\frac{1}{2}$ is multiplied to account for the two channel walls.

The interfacial tension, γ, according to the thermodynamic definition, is the isothermal work required to increase the interface by unit area, i.e., $\gamma = \frac{1}{2}\left(\frac{\partial \Omega}{\partial A}\right)_{T,\mu,H}$ for a slit-channel system. Alternatively, γ can also be determined, according to the mechanical definition, in terms of the stress transmitted across a strip of unit width normal to the interface. In this work, we use a mechanical definition of the surface tension given by [52]

$$\gamma(H) = \frac{1}{2}\int_0^H (P_{\mathrm{n}}(z) - P_l(z))\, dz, \tag{4.12}$$

where $P_{\mathrm{n}}(z)$ and $P_l(z)$ are the normal and lateral components of the local pressure tensor. In a bulk fluid, pressure is homogeneous and isotropic, however, in a confined fluid, pressure varies with the position and is anisotropic due to the wall-fluid force field and local variations in the fluid density [53, 54, 55]. For a slit-channel system, $P_l(z)$ can be computed as a negative of the local grand potential density, $\Omega(z)$ [56, 57].

Also, for a slit-channel system in the steady-state, $P_{\mathrm{n}}(z)$ must be uniform across the channel width to satisfy a mechanical equilibrium condition. Therefore, for a given channel of width H, an average normal pressure value, $P_{\mathrm{n}}(H)$, can be computed using the thermodynamic definition as

$$P_{\mathrm{n}}(H) = -\frac{1}{A}\frac{\partial \Omega}{\partial H} \tag{4.13}$$

To compute $\partial\Omega(H)/\partial H$ in Eq. 4.13, we use the central difference scheme as

$$P_{\mathrm{n}}(H) = -\frac{1}{A}\frac{\Omega(H+\epsilon) - \Omega(H-\epsilon)}{2\epsilon} \tag{4.14}$$

where ϵ is the infinitesimal change in the channel width.

The solvation force, f_{S}, is the difference between the pressure exerted by a confined fluid on the channel walls and the bulk fluid pressure, P_{b} [58, 59]. For a slit-like system in mechanical equilibrium, the pressure exerted by a confined fluid on the channel walls is equal to the average normal pressure, $P_{\mathrm{n}}(L)$. Therefore, the solvation force can be computed as

$$f_{\mathrm{S}}(L) = P_{\mathrm{n}}(L) - P_{\mathrm{b}} \tag{4.15}$$

4.3 Classical density functional theory

cDFT is a continuum-based technique that describes the properties of inhomogeneous fluids from a microscopic level [58, 25, 60]. It is based on the theorem that, for a fluid in an external field, the Helmholtz free energy, F, is a unique functional of the average molecular density profile, $\rho(\mathbf{r})$, independent of the external potential, $V_{\text{ext}}(\mathbf{r})$ [58, 25, 60]. Therefore, in cDFT, the grand potential is defined as a functional of $\rho(\mathbf{r})$:

$$\Omega\left[\rho(\mathbf{r})\right] = F\left[\rho(\mathbf{r})\right] + \int \left(V_{\text{ext}}(\mathbf{r}) - \mu\right)\rho(\mathbf{r})d\mathbf{r}. \tag{4.16}$$

To determine Ω from Eq. 4.16, we require an expression for $F\left[\rho(\mathbf{r})\right]$. The Helmholtz energy has two parts: (i) the ideal part, $F^{\text{id}}\left[\rho(\mathbf{r})\right]$, and (ii) the excess part, $F^{\text{ex}}\left[\rho(\mathbf{r})\right]$, i.e.,

$$F\left[\rho(\mathbf{r})\right] = F^{\text{id}}\left[\rho(\mathbf{r})\right] + F^{\text{ex}}\left[\rho(\mathbf{r})\right]. \tag{4.17}$$

The ideal part of the Helmholtz energy accounts for the ideal gas free energy,

$$F^{\text{id}}\left[\rho(\mathbf{r})\right] = k_{\text{B}}T\int \rho(\mathbf{r})\left(\ln\left(\rho(\mathbf{r})\Lambda^3\right) - 1\right)d\mathbf{r}, \tag{4.18}$$

where k_{B} is the Boltzmann constant, $\Lambda = \left(\frac{2\pi\hbar^2}{mk_{\text{B}}T}\right)^{\frac{1}{2}}$ is the thermal wavelength, $\hbar$ is the reduced Planck's constant, and m is the mass of an atom. The excess part of the intrinsic Helmholtz energy accounts for the non-bonded interactions between molecules. Modeling the excess free energy is the most challenging part of the cDFT. The exact expression for $F^{\text{ex}}\left[\rho(\mathbf{r})\right]$ is in general unknown [60]. There exists approximate functionals for $F^{\text{ex}}\left[\rho(\mathbf{r})\right]$, such as fundamental-measure theory (FMT) functionals [61, 62, 63, 64, 65, 66] and functionals based on the statistical associating fluid theory (SAFT) [67, 68, 69].

According to the variational principle

$$\left.\frac{\delta\Omega\left[\rho(\mathbf{r})\right]}{\delta\rho}\right|_{eq} = 0, \tag{4.19}$$

and therefore the equilibrium density distribution satisfies

$$\rho(\mathbf{r}) = \rho_{\text{b}}\exp\left(-\frac{1}{k_{\text{B}}T}\left[V_{\text{ext}}(\mathbf{r}) + \frac{\delta F^{\text{ex}}\left[\rho(\mathbf{r})\right]}{\delta\rho(\mathbf{r})} - \mu^{\text{ex}}\right]\right), \tag{4.20}$$

where the bulk chemical potential μ has been decomposed into ideal (μ^{id}) and excess (μ^{ex}) part. In Eq. 4.20, we use the fact that the system is in equilibrium with the bulk reservoir; thus, ideal part of chemical potential can be related to the bulk density (ρ_b). To show this, we use the relation between the ideal

chemical potential and ideal free energy given by

$$\mu_b^{\mathrm{id}} = \left.\frac{\partial F_b^{\mathrm{id}}}{N_b}\right|_T \tag{4.21}$$

where N_b is the number of particles in the bulk phase. Using the same expression given for the ideal free energy in Eq. 4.18 for the bulk, Eq. 4.22 can be related to the bulk density as follows,

$$\mu_b^{\mathrm{id}} = k_B T \log\left(\rho_b \Lambda^3\right). \tag{4.22}$$

In the following section, we use EQT to formulate $F^{\mathrm{ex}}\left[\rho(\mathbf{r})\right]$ so that we get a closed from of Eq. 4.20.

4.4 EQT-cDFT for confined single component LJ fluids

In the EQT-cDFT approach, the fluid-fluid EQT potential model (Eq. 3.25) is used to construct the excess part of the intrinsic Helmholtz energy functional as

$$F^{\mathrm{EQT,ex}}\left[\rho(\mathbf{r})\right] = \frac{1}{2}\int \rho(\mathbf{r}')U^{\mathrm{ff}}(\mathbf{r}')d\mathbf{r}'. \tag{4.23}$$

Following the same formula in Eq. 3.25, in the bulk phase the EQT fluid-fluid potential can be written as follows:

$$U_b^{\mathrm{ff}} = 4\pi\rho_b \int r^2 \left(u^{\mathrm{ff}}(|\mathbf{r}-\mathbf{r}'|)g^{\mathrm{hs}}(|\mathbf{r}-\mathbf{r}'|) + u_{\mathrm{ccp}}^{\mathrm{ff}}(|\mathbf{r}-\mathbf{r}'|)\right) dr. \tag{4.24}$$

Similar to Eq. 4.23, we can construct the bulk excess free energy by using Eq. 4.24,

$$F_b^{\mathrm{EQT,ex}}\left[\rho(\mathbf{r})\right] = \frac{1}{2}\int \rho_b U_b^{\mathrm{ff}} d\mathbf{r} = \frac{V}{2}\rho_b U_b^{\mathrm{ff}} \tag{4.25}$$

where V is the volume of the fluid in the bulk phase. Similar to what we did for the ideal part of the chemical potential, the excess part in Eq. 4.20 is equal to the bulk excess chemical potential and can be related to the excess free energy as

$$\mu_b^{\mathrm{ex}} = \left.\frac{\partial F_b^{\mathrm{ex}}}{N_b}\right|_T \tag{4.26}$$

Using Eqs. 4.25 and 4.26, it is easy to show that $\mu_b^{\mathrm{ex}} = U_b^{\mathrm{ff}}$ and by substituting $V_{\mathrm{ext}}(\mathbf{r}) = U^{\mathrm{wf}}(\mathbf{r})$, Eq. 4.20 can be re-written in terms of the EQT formulation:

$$\rho(\mathbf{r}) = \rho_{\mathrm{b}} \exp\left(-\frac{1}{k_{\mathrm{B}}T}\left(U^{\mathrm{ff}}(\mathbf{r}) + U^{\mathrm{wf}}(\mathbf{r}) - U_{\mathrm{b}}^{\mathrm{ff}}\right)\right). \tag{4.27}$$

Therefore, in the EQT-cDFT approach, one can obtain the equilibrium density and potential profiles of a confined fluid using a numerical procedure such

as Picárd iteration to self-consistently solve Eqs. 3.6, 3.25, and 4.27. Unlike the Nernst-Planck approach (Eq. 3.1), EQT-cDFT approach eliminates the requirement for a-priori knowledge of the average density, ρ_{avg}, for each channel. Instead, ρ_{avg} can be obtained as an output of this method for various channel widths.

Finally, to obtain the thermodynamic properties from EQT-cDFT approach, we need an expression for the grand potential. From Eqs. 4.17, 4.18, 4.23, 3.6, and 4.16, we get the EQT-cDFT-based grand potential functional, $\Omega^{\text{EQT}}[\rho(\mathbf{r})]$, as

$$\begin{aligned}\Omega^{\text{EQT}}[\rho(\mathbf{r})] &= k_{\text{B}}T\int \rho(\mathbf{r})\left(\ln\left(\rho(\mathbf{r})\Lambda^3\right)-1\right)d\mathbf{r} \\ &\quad +\frac{1}{2}\int \rho(\mathbf{r})U^{\text{ff}}(\mathbf{r})d\mathbf{r} \\ &\quad +\int \left(U^{\text{wf}}(\mathbf{r})-\mu\right)\rho(\mathbf{r})d\mathbf{r},\end{aligned} \tag{4.28}$$

where μ is given by

$$\mu = k_{\text{B}}T\log\left(\rho_{\text{b}}\Lambda^3\right)+U_{\text{b}}^{\text{ff}}. \tag{4.29}$$

Using Eq. 4.28 and the relations mentioned in Section 4.2, one can obtain various thermodynamic properties for a confined fluid in a slit-channel. For instance, the lateral pressure variation along the z-direction can be obtained from the following relation:

$$\begin{aligned}P_l(z) &= -k_{\text{B}}T\rho(z)\left(\ln\left(\rho(z)\Lambda^3\right)-1\right) \\ &\quad -\frac{1}{2}\rho(z)U^{\text{ff}}(z) \\ &\quad -\left(U^{\text{wf}}(z)-\mu\right)\rho(z).\end{aligned} \tag{4.30}$$

Using Eqs. 4.29 and 4.27 in Eq. 4.30, Eq. 4.30 simplifies to

$$P_l(z) = \rho(z)k_BT+\frac{1}{2}\rho(z)U^{\text{ff}}(z). \tag{4.31}$$

In Eq. 4.31 the first term refers to the kinetic part of the pressure and the second term refers to the contributions from vdw part of the fluid-fluid interactions.

4.5 EQT-cDFT for confined multi-component LJ mixtures

In this section, we extend EQT-cDFT formalism to a multi-component system. For such a system in presence of an external potential, $V_{\text{ext},\alpha}$, Ω is written as

$$\Omega\left[\{\rho_\alpha(\mathbf{r})\}\right] = F^{\text{id}}\left[\{\rho_\alpha(\mathbf{r})\}\right] + F^{\text{ex}}\left[\{\rho_\alpha(\mathbf{r})\}\right] + \sum_{\alpha=1}^{m}\int\left[V_{\text{ext},\alpha}(\mathbf{r}) - \mu_\alpha\right]\rho_\alpha(\mathbf{r})d\mathbf{r}, \tag{4.32}$$

where for the mixtures, the ideal part of the intrinsic Helmholtz free energy is given by

$$F^{\text{id}}\left[\{\rho_\alpha(\mathbf{r})\}\right] = k_{\text{B}}T\sum_{\alpha=1}^{m}\int\rho_\alpha(\mathbf{r})\left(\ln\left(\rho_\alpha(\mathbf{r})\Lambda_\alpha^3\right) - 1\right)d\mathbf{r}. \tag{4.33}$$

As mentioned in Section 4.3, in general, the exact expression for the excess free energy is unknown, and there exist approximations to model this part of the free energy. Following the same procedure as for EQT-cDFT of the single component case, the equilibrium density distribution for each fluid component satisfies

$$\rho_\alpha(\mathbf{r}) = \rho_{\alpha,\text{b}}\exp\left(-\frac{1}{k_{\text{B}}T}\left[V_{\alpha,\text{ext}}(\mathbf{r}) + \frac{\delta F^{\text{ex}}\left[\{\rho_\alpha(\mathbf{r})\}\right]}{\delta\rho_\alpha(\mathbf{r})} - \mu_\alpha^{\text{ex}}\right]\right), \tag{4.34}$$

In the EQT-cDFT, as in Eq. 4.23 we model the excess free energy in Eq. 4.34 as

$$F^{\text{EQT,ex}}\left[\{\rho_\alpha(\mathbf{r})\}\right] = \frac{1}{2}\sum_{\alpha=1}^{m}\int\rho_\alpha(\mathbf{r}')U_\alpha^{\text{ff}}(\mathbf{r}')d\mathbf{r}'. \tag{4.35}$$

Using Eq. 4.35, Eq. 4.26, and substituting $V_{\text{ext},\alpha} = U_\alpha^{\text{wf}}$, we can rewrite Eq. 4.34 in terms of EQT formulation:

$$\rho_\alpha(\mathbf{r}) = \rho_{\alpha,\text{b}}\exp\left(-\frac{1}{k_{\text{B}}T}\left(U_\alpha^{\text{ff}}(\mathbf{r}) + U_\alpha^{\text{wf}}(\mathbf{r}) - U_{\alpha,\text{b}}^{\text{ff}}\right)\right). \tag{4.36}$$

where $U_{\alpha,b}^{\text{ff}}$ is the bulk potential energy per particle for each component, and it is given by

$$U_{\alpha,b}^{\text{ff}} = 4\pi\sum_{\beta=1}^{m}\rho_{\beta,b}\int r^2\left(u_{\alpha\beta}^{\text{ff}}(|\mathbf{r}-\mathbf{r}'|)g_{\alpha\beta}^{\text{hs}}(|\mathbf{r}-\mathbf{r}'|) + u_{\text{ccp},\alpha\beta}^{\text{ff}}(|\mathbf{r}-\mathbf{r}'|)\right)dr. \tag{4.37}$$

CHAPTER 5

RESULTS

In this chapter, we investigate the accuracy of the EQT-cDFT approach against the reference all-atom MD simulations for various channel widths. For this purpose, first we provide results for single component LJ fluid systems namely, methane-graphene and argon-graphene slit-channel systems. Next, we show structural properties from MD and EQT-cDFT approach of the binary mixtures of methane and hydrogen molecules confined in graphitic slit channels. As mentioned in Section 2.3, to demonstrate the applicability of the EQT-cDFT approach for confined fluid mixtures we consider two different bulk mixture compositions. One contains high concentration of hydrogen molecules (x_h = 0.3) and the other reservoir is rich in methane (x_m = 0.7). For both single- and multi-component cases, all the channels are in equilibrium with their bulk reservoirs. To find out more about the MD simulation setups and different ensembles, please see chapter 2.

5.1 Single component LJ fluid

In the EQT-cDFT simulations of methane-graphene and argon-graphene slit-channel systems, we model $u^{\text{wf}}(r)$ and $u^{\text{ff}}(r)$ as the standard 12-6 LJ potentials. For the methane-graphene, argon-graphene, methane-methane, and argon-argon LJ interactions, we use the same LJ parameters as in the MD simulations that are given in Table 2.2. The average densities of fluid molecules used both in MD and EQT-cDFT approach, i.e., ρ_{avg} = no. of molecules/volume of the channel, in various size channels are given in Table 5.1.

Table 5.1: Average fluid densities (nm^{-3}) in MD simulations of various size channels.

System	20σ	15σ	10σ	9σ	6σ	3σ	2σ
Methane-graphene	17.18	16.92	16.37	16.20	15.24	11.94	9.09
Argon-graphene	22.76	22.30	21.50	21.24	19.84	15.79	12.05

The cut-offs for the wall-fluid, $R^{\text{wf}}_{\text{cut}}$, and fluid-fluid, $R^{\text{ff}}_{\text{cut}}$, pair interactions are set to $1.4nm$. For the cubic B-splines-based $u^{\text{ff}}_{\text{ccp}}(r)$ (Eq. 3.26), we use $\Delta r = 0.04$ nm and $n = 36$ and optimize the spline knot values, $\{c_0, c_1, c_2, ..., c_{n+1}\}$, using

a systematic approach based on the potential of mean force (PMF) matching (Eq. 3.30). Modeling correlation-correction potential using B-splines (Eq. 3.26) gives flexibility to the correction function and provide a numerically robust way of obtaining accurate density profiles. Here, to optimize the spline knot values of $u^{\text{ff}}_{\text{ccp}}(r)$ for methane and argon, we use the corresponding 20σ channel atomistic trajectories from the MD simulation as a reference. Fig. 5.1 shows the optimized $u^{\text{ff}}_{\text{ccp}}(r)$ for the methane-methane and argon-argon interactions. Although, correlation-correction potentials are optimized for a reference channel of width 20σ, we find that they are transferrable across different pores at the same thermodynamic state. This can be due to fact that PMF-matching approach optimizes structurally consistent potential parameters at the specific thermodynamic state.

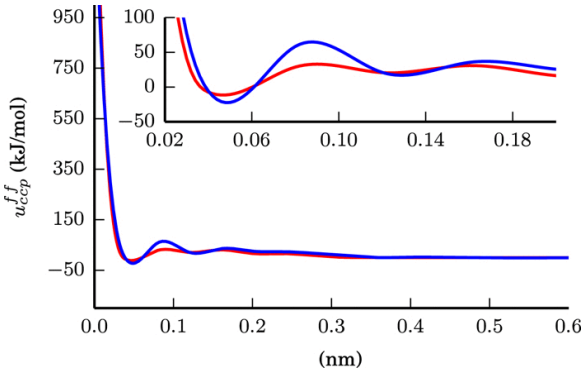

Figure 5.1: Fluid-fluid correlation correction potentials: methane-methane (blue) and argon-argon (red).

To obtain equilibrium density profiles of methane and argon inside graphene-slit channels of various widths, we self-consistently solve Eqs. 3.6, 3.25, and 4.27. Fig. 5.2 shows that, for both methane-graphene and argon-graphene systems, the equilibrium density profiles from the EQT-cDFT agree well with the MD simulations for various channel widths. We observe that the methane and argon density profiles are similar and oscillatory, because the confined LJ fluid molecules arrange in the layers near the walls due to the competition between the wall-fluid and fluid-fluid interactions. When $H = 3\sigma$, fluid molecules arrange in two layers located around 0.95σ distance from each wall. A layer of particles is added mid-way between the walls with each σ increase in the channel width, and the density of the added layer decreases with increase in the distance from the walls. The maximum number of layers occur when $H = 18\sigma$. Further increase in H only adds flat bulk-like region in the middle of a channel.

Fig. 5.3 shows the variation of ρ_{avg} and Γ with H. We observe that, for the channels 2σ to 20σ, $\Gamma < 0$ and $\rho_{\text{avg}} < \rho_{\text{b}}$. Due to the strong repulsion from the wall atoms, fluid molecules cannot access the volume very close to the walls. Moreover, the layering of particles not only forms the regions of high ($> \rho_{\text{b}}$) densities, but also the regions of low ($< \rho_{\text{b}}$) densities inside a channel.

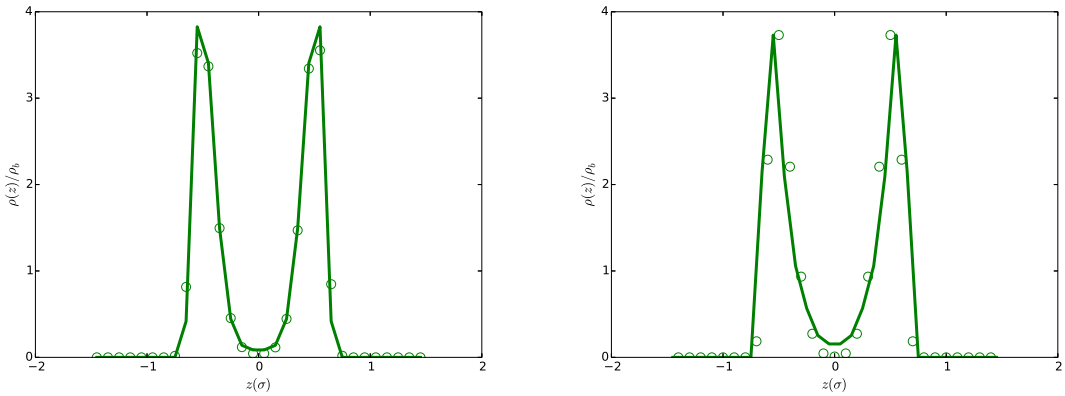

(a) (b)

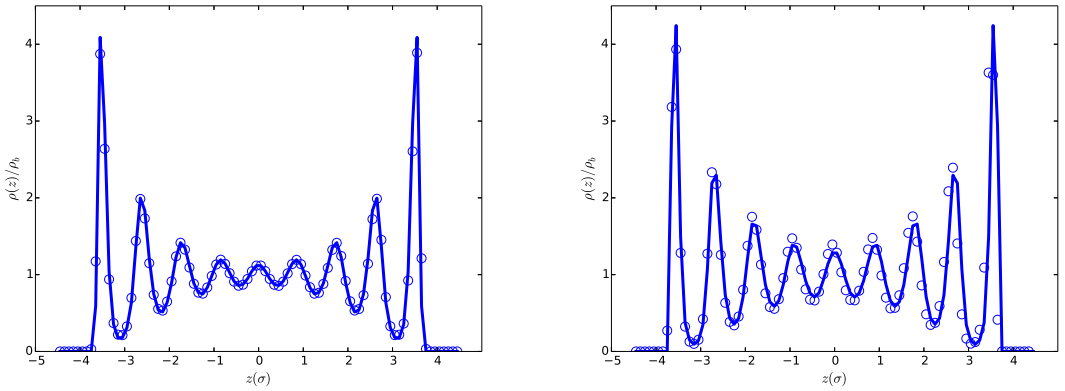

(c) (d)

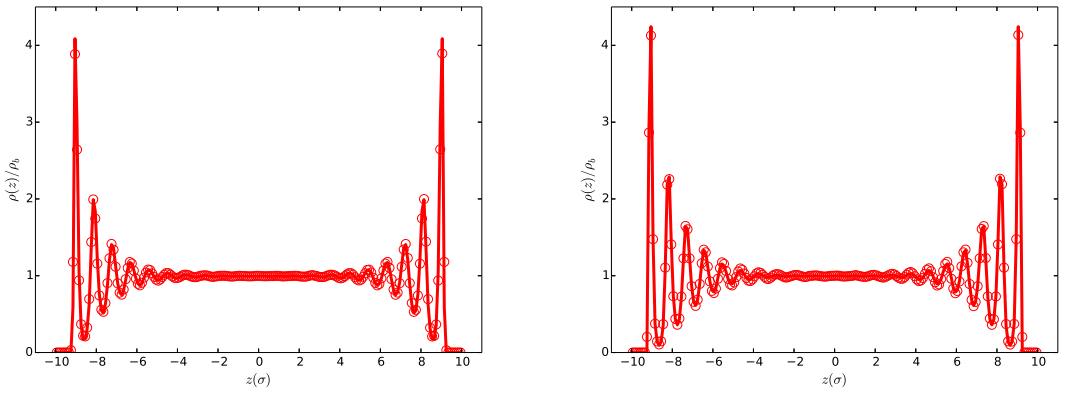

(e) (f)

Figure 5.2: Comparison of density profiles of argon (a,c,e) and methane (b,d,f) from EQT-cDFT (lines) and MD (circles) simulations at different channel widths: 20σ (red), 9σ (blue), and 3σ (green).

The net effect of the excluded volume and layering is that the total number of fluid molecules inside the channel of a volume V is smaller than the number of molecules in the bulk of the same volume. We also observe that, for the smaller channels with no bulk-like region, Γ oscillates with H. The oscillations in Γ follow the formations of adsorbed layers with increasing H. The minimum in Γ occur when adsorbed particles form an additional layer to arrange in a closely packed structure and reduce the average density.

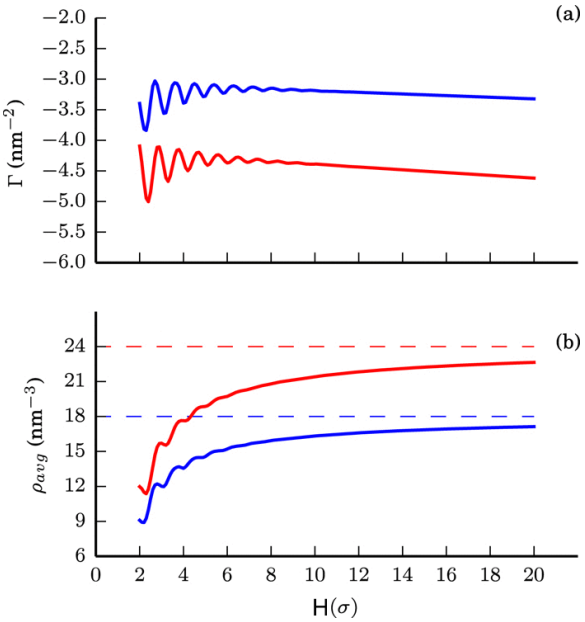

Figure 5.3: EQT-cDFT predictions for total adsorption (a) and average density (b) of methane (blue solid lines) and argon (red solid lines) molecules inside graphene slit channels of various widths. In subfigure (b) dotted lines correspond to the bulk densities of methane (blue) and argon (red).

Next, we compute the local pressure tensor, surface tension, and solvation force. To compute the local pressure tensors from MD, we use the method of Schofield and Henderson [70] in combination with the Gaussian smoothing kernel similar to ref. [54]. The local pressure determination method is not available in the default GROMACS 4.6.1 version. Therefore, for this work, we modified the GROMACS source code and implemented the method for determining the local pressure tensor in a slit-like geometry. Our implementation of the local pressure tensor method in GROMACS is publicly available on GitHub [71]. Recently, Vanegas et al. [72] have also implemented a local pressure calculation method in a custom version of GROMACS, which is based on the Hardy–Murdoch procedure. The surface tension and solvation force values from MD are determined by substituting the MD local pressure values in Eqs. 4.12 and 4.15, respectively. To estimate the errors in the properties from MD, we perform 5 different MD simulations with different initial conditions and obtain 5 sets of mean values of the properties. The estimate of error in the properties from MD are found to

be less than 1.0%.

Fig. 5.4 shows the lateral pressure profiles in the methane-graphene and argon-graphene systems. It can be observed that the lateral pressure predictions from the EQT-cDFT compare well with the MD for various channel widths. We observe that, in a channel, $P_l(z)$ oscillates similar to $\rho(z)$. The lateral pressure values are much higher near the walls than the bulk pressure. The maximum value of $P_l(z)$ occurs near the first density peak, i.e., 0.95σ from the walls, and it is ≈ 5 times greater than the bulk pressure. Such high pressures in a confined fluid near the channel walls provide explanations for the confined fluid nanophases[73, 14], such as high pressure solid phases [74, 75] and chemical reactions [12]. Away from the walls, the oscillations in $P_l(z)$ decay towards the bulk value.

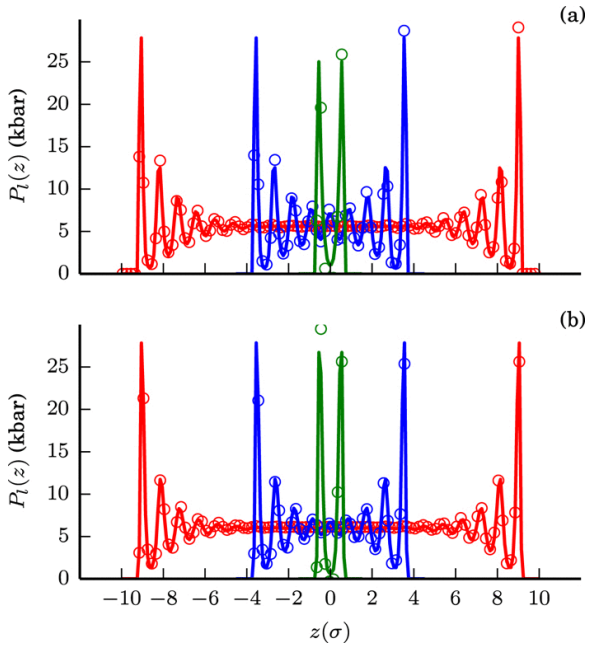

Figure 5.4: Comparison of lateral pressure profiles of methane (a) and argon (b) from EQT-cDFT (lines) and MD (circles) simulations for various channel widths: 20σ (red), 9σ (blue), and 3σ (green).

Fig. 5.5 shows the variation of the normal pressure, surface tension, and solvation force as a function of H for both methane-graphene and argon-graphene systems. We observe that the predictions for $P_{\rm n}(H)$, $\gamma(H)$, and $f_{\rm S}(H)$ from the EQT-cDFT simulations compare well with the MD simulations. Fig. 5.5 shows that the normal pressure oscillates with H for channels less than 9σ and it approaches the bulk pressure value for $H > 9\sigma$. The oscillations in the normal pressure are well-known and they arise because of the oscillations in the average density values (see Fig. 5.3) [59, 74, 73, 53, 14]. Similar to the normal pressure, the surface tension and solvation force oscillate for the smaller channels and the amplitudes of oscillations decay rapidly with increasing H.

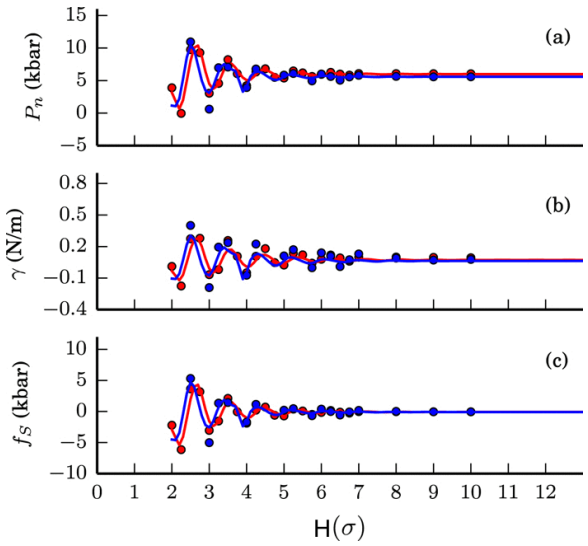

Figure 5.5: Variation of normal pressure (a), surface tension (b), and solvation force (c) of methane (blue) and argon (red) with channel width. Lines are EQT-cDFT results and circles are MD results.

5.2 Multi-component LJ fluid mixture

In the EQT-cDFT simulations for confined binary mixture of hydrogen and methane molecule, we model $u^{\text{wf}}(r)$ and $u^{\text{ff}}(r)$ as the standard 12-6 LJ potentials. For the methane-graphene, hydrogen-graphene, methane-methane, hydrogen-methane and hydrogen-hydrogen LJ interactions, we use the same LJ parameters as in the MD simulations that are given in Table 2.3.

As mentioned in Section 4.4, the average concentration in the channels can be predicted by the EQT-cDFT approach. To examine this, in MD simulations linear superposition approximation (LSA) method [76] is adopted to estimate the number of molecules inside the channels of width larger than 1.524 nm ($= 4\sigma_{22}$). It has been shown that LSA results in constant chemical potential except at very small separations (about two molecular diameters)[77]. Hence, for pores smaller than $4\sigma_{22}$, the EQT-cDFT results are verified by NVT simulation of slit channels in contact with bulk mixture [29]. The distance between walls, densities and correlation-correction potentials are made dimensionless based on hydrogen LJ parameters (σ_{11}, ϵ_{11}) and represented by $z^* = z/\sigma_{11}$, $\rho^*_\alpha = \rho_\alpha \sigma^3_{11}$, and $(u^{\text{ff}}_{\text{ccp},\alpha\beta})^* = u^{\text{ff}}_{\text{ccp},\alpha\beta}/\epsilon_{11}$, respectively.

We optimize methane-methane, methane-hydrogen, hydrogen-hydrogen, and hydrogen-methane correlation-correction potentials for each bulk mixture composition considered in this work. For each bulk mixture composition, PMF-matching-based optimization is performed using the methane and hydrogen density profiles in 6.34 nm channel, which are obtained from the reference MD simulations. We choose 6.34 nm channel for optimization because it is large enough that the layered structure and bulk region are well formed for both

hydrogen and methane. Fig. 5.6 shows the optimized $(u_{\rm ccp}^{\rm ff})^*$ for different fluid-fluid interactions. Similar to the single component case, we observed that the correlation-correction potentials that are optimized for a reference channel of 6.34 nm width, are transferrable across different pores at the same thermodynamic state.

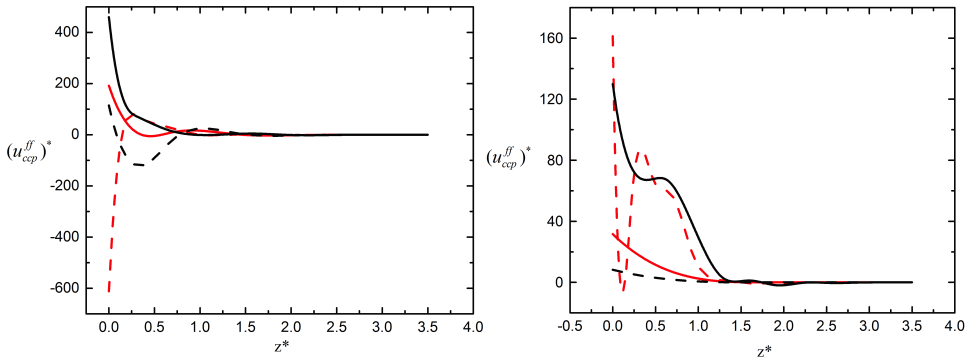

(a) (b)

Figure 5.6: Correlation-correction potentials for $x_m = 0.3$ (a) and $x_m = 0.7$ (b) bulk compositions. Solid lines represent alike interactions: CH_4 - CH_4 (black), H_2 - H_2 (red); Dashed lines stand for cross interactions: CH_4 - H_2 (black), H_2 - CH_4 (red).

Figs. 5.7 and 5.8, depict that the density profiles from the quasi-continuum framework agree well with the MD simulations. In all cases, except for the hydrogen density profile in the smallest channel of methane bulk composition of 0.3 (see Fig. 5.7a), the EQT-cDFT predictions are as accurate as MD. Both methane and hydrogen molecules arrange in layers and exhibit an oscillatory structural behavior due to the interplay of wall-fluid and fluid-fluid interactions. Well-formed layered structure and a plateau bulk region are observed for both hydrogen and methane in 6.34 nm channel, which is the largest channel considered in this study (see Figs. 5.7f and 5.8f). Layering is enhanced as the bulk composition increases from 0.3 to 0.7 (Compare Figs. 5.7b-5.7f and 5.8b-5.8f). This fact is more evident by comparing number of layers for methane and hydrogen in a slit width of 3.21nm (see Figs. 5.7d and 5.8d). The number of layers for methane and hydrogen of bulk composition 0.3 are 6 whereas for bulk mixture of 0.7, methane and hydrogen molecules are arranged in 8 layers. Thus, increasing methane mole fraction enhances the structural order for both methane and hydrogen. Finally, by comparing the magnitude of the first peak for methane and hydrogen densities, it is evident that methane molecules are more concentrated in the vicinity of the wall.

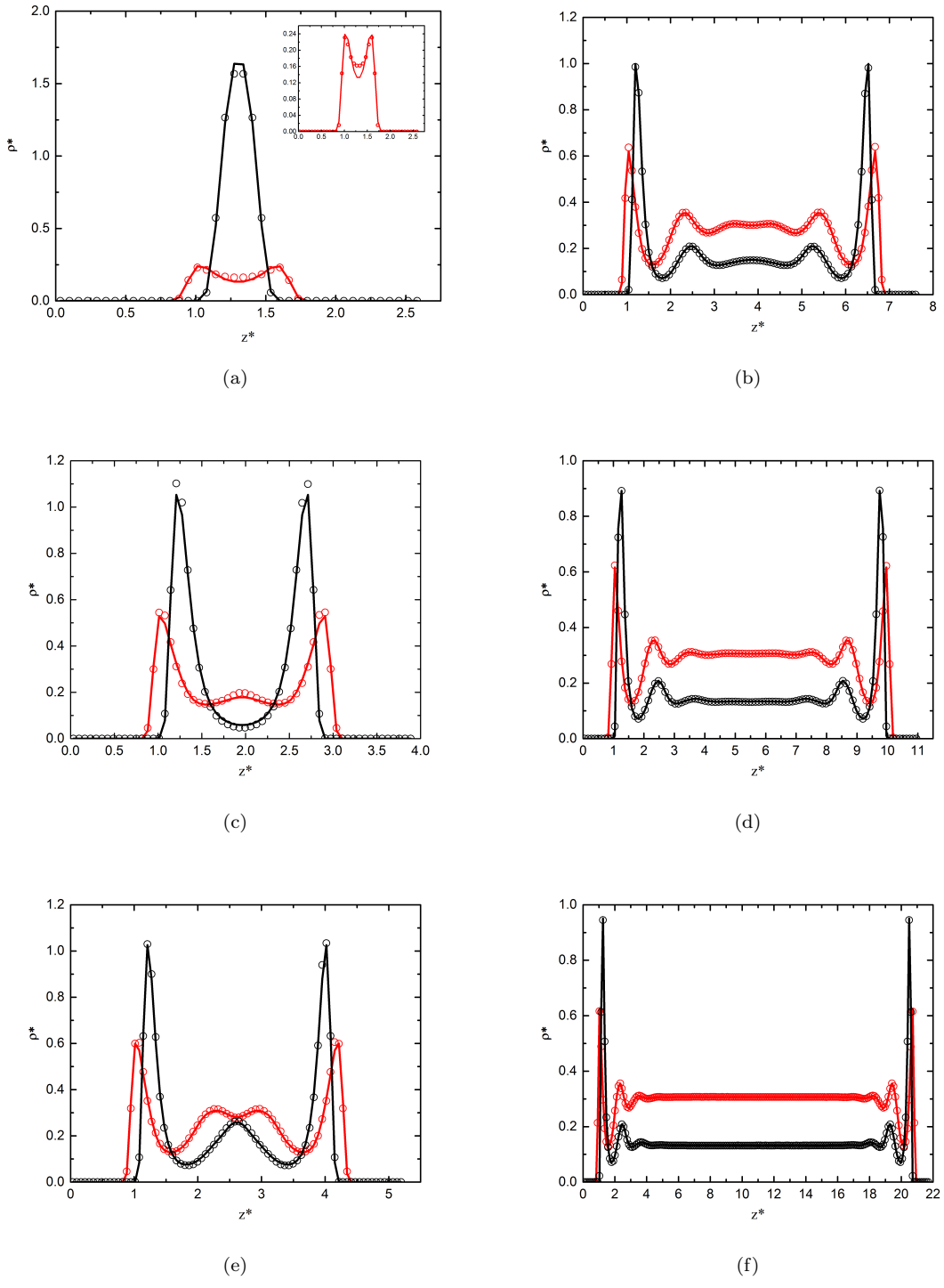

Figure 5.7: Comparison of the density profiles of methane and hydrogen from EQT-cDFT and MD simulations at $T = 300$ K for various channel widths in equilibrium with hydrogen-rich bulk mixture (x_m= 0.3): a) 0.762 nm, b) 2.25 nm, c) 1.143 nm, d) 3.21 nm, e) 1.524 nm, f) 6.34 nm. In all subfigures, circles are MD and lines are EQT-cDFT simulation results in which red and black colors denote hydrogen and methane densities, respectively.

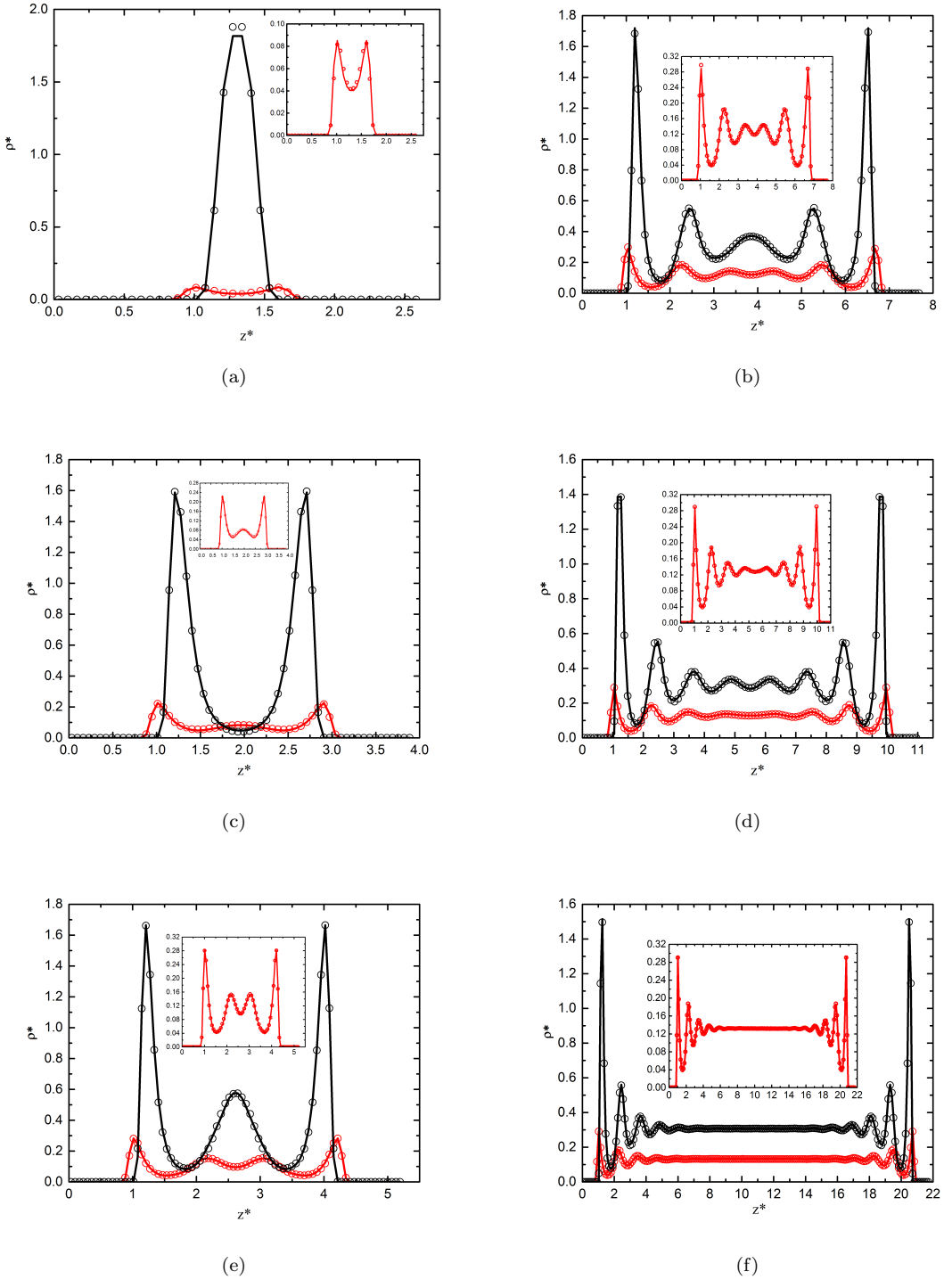

Figure 5.8: Comparison of the density profiles of methane and hydrogen from EQT-cDFT and MD simulations at $T = 300$ K for various channel widths in equilibrium with methane-rich bulk mixture (x_m= 0.7): a) 0.762 nm, b) 2.25 nm, c) 1.143 nm, d) 3.21 nm, e) 1.524 nm, f) 6.34 nm. In all subfigures, circles are MD and lines are EQT-cDFT simulation results in which red and black colors denote hydrogen and methane densities, respectively.

The essential new feature for mixtures is the change in composition due to confinement. Depending on the width, structure and material, nanopore may become selective towards a certain fluid component in the mixture. This selectivity, S, is often expressed as [13, 44, 78]

$$S = \frac{x^{\text{pore}}_{\text{CH}_4}/x^{\text{bulk}}_{\text{CH}_4}}{x^{\text{pore}}_{\text{H}_2}/x^{\text{bulk}}_{\text{H}_2}} \tag{5.1}$$

where x^{pore} and x^{bulk} represent the fluid mole fraction in the pore and the bulk phase, respectively. Fig. 5.9 shows the selectivity for hydrogen-rich bulk mixture as a function of pore width. S values less than unity represent that the channel is selective toward hydrogen while the values greater than unity imply favorability for methane. It can be seen in Fig. 5.9 that methane shows a higher adsorption affinity than hydrogen, especially in the smaller pores. This is due to the larger interaction energy between methane and graphene than hydrogen. The same line of reasoning has also been used in other literature [79, 80] in which they have shown that the molar fraction of the component having the strongest interaction with the channel is increased compared to the bulk.

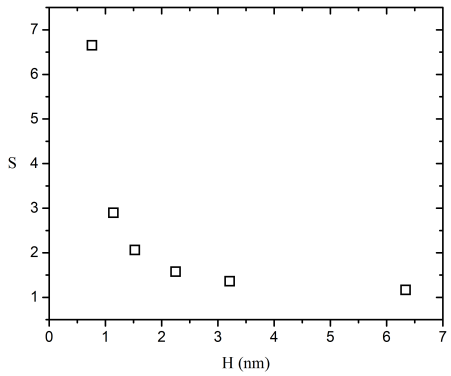

Figure 5.9: Selectivity of methane over hydrogen as a function of channel width.

CHAPTER 6

CONCLUSION AND FUTURE WORK

EQT is a practical, fast and easy approach to bridge the gap between atomistic and continuum methods by constructing potentials from atomistic interactions. These potentials can be used in a continuum framework such as the Nernst-Planck equation or to construct a grand potential functional within the classical density functional theory framework (EQT-cDFT). In the present study, we demonstrated the EQT-cDFT approach for the single component LJ fluids, methane and argon, and multi-component LJ fluids, binary mixture of methane and hydrogen molecules, confined in slit-like graphene channels of various widths. The EQT-cDFT predictions for the structure and thermodynamic properties, like the density, adsorption, local pressure tensor, surface tension, and solvation force, compare well with the MD simulations. For confined LJ fluid mixtures, we considered two extreme cases, where channels are in equilibrium with methane-rich and hydrogen-rich bulk mixtures. In both cases, theoretical results compare well with the MD simulations. We also used EQT-cDFT results to calculate adsorption selectivity of the mixture rich in hydrogen. It is found that, though the bulk composition favors hydrogen, graphene slit channels exhibit selectivity for methane molecule. This finding can be attributed to the larger energy interaction of methane and graphene wall. EQT-cDFT is a promising multiscale framework that can accurately predict structure and other thermodynamic properties of confined fluids.

There is no limitation to EQT in terms of system complexity. It has been shown that, EQT can also capture density variation of polar molecules such as water in nanoconfined channels [38]. In fact, EQT framework also provides a tool to use particle-based coarse-grained potentials for which the electrostatic effects are already imbedded. Thus, Complex systems that involve long-range electrostatic interactions such as water/methanol mixtures and electrolytes can also be investigated and studies in these directions are in progress.

REFERENCES

[1] M. Suk, A. Raghunathan, and N. Aluru, "Fast reverse osmosis using boron nitride and carbon nanotubes," *Applied Physics Letters*, vol. 92, no. 13, p. 133120, 2008.

[2] J. Han, J. Fu, and R. B. Schoch, "Molecular sieving using nanofilters: past, present and future," *Lab on a Chip*, vol. 8, no. 1, pp. 23–33, 2008.

[3] K. P. Lee, T. C. Arnot, and D. Mattia, "A review of reverse osmosis membrane materials for desalinationdevelopment to date and future potential," *Journal of Membrane Science*, vol. 370, no. 1, pp. 1–22, 2011.

[4] N. Hilal, H. Al-Zoubi, N. Darwish, A. Mohamma, and M. A. Arabi, "A comprehensive review of nanofiltration membranes: Treatment, pretreatment, modelling, and atomic force microscopy," *Desalination*, vol. 170, no. 3, pp. 281–308, 2004.

[5] A. Bhattacharya and P. Ghosh, "Nanofiltration and reverse osmosis membranes: theory and application in separation of electrolytes," *Reviews in Chemical Engineering*, vol. 20, no. 1-2, pp. 111–173, 2004.

[6] P. T. Cummings, H. Docherty, C. R. Iacovella, and J. K. Singh, "Phase transitions in nanoconfined fluids: The evidence from simulation and theory," *AIChE journal*, vol. 56, no. 4, pp. 842–848, 2010.

[7] C. Smith, "Tools for drug discovery: Tools of the trade," *Nature*, vol. 446, no. 7132, pp. 219–222, 2007.

[8] B. Suleimanov, F. Ismailov, and E. Veliyev, "Nanofluid for enhanced oil recovery," *Journal of Petroleum Science and Engineering*, vol. 78, no. 2, pp. 431–437, 2011.

[9] D. Wever, F. Picchioni, and A. Broekhuis, "Polymers for enhanced oil recovery: a paradigm for structure–property relationship in aqueous solution," *Progress in Polymer Science*, vol. 36, no. 11, pp. 1558–1628, 2011.

[10] S. Kandlikar, S. Garimella, D. Li, S. Colin, and M. R. King, *Heat transfer and fluid flow in minichannels and microchannels*. Elsevier, 2005.

[11] X. Liang, "Some effects of interface on fluid flow and heat transfer on micro- and nanoscale," *Chinese Science Bulletin*, vol. 52, no. 18, pp. 2457–2472, 2007.

[12] K. Urita, Y. Shiga, T. Fujimori, T. Iiyama, Y. Hattori, H. Kanoh, T. Ohba, H. Tanaka, M. Yudasaka, S. Iijima et al., "Confinement in carbon nanospace-induced production of ki nanocrystals of high-pressure phase," *Journal of the American Chemical Society*, vol. 133, no. 27, pp. 10 344–10 347, 2011.

[13] L. D. Gelb, K. Gubbins, R. Radhakrishnan, and M. Sliwinska-Bartkowiak, "Phase separation in confined systems," *Reports on Progress in Physics*, vol. 62, no. 12, p. 1573, 1999.

[14] Y. Long, J. C. Palmer, B. Coasne, M. Śliwinska-Bartkowiak, G. Jackson, E. A. Müller, and K. E. Gubbins, "On the molecular origin of high-pressure effects in nanoconfinement: The role of surface chemistry and roughness," *The Journal of chemical physics*, vol. 139, no. 14, p. 144701, 2013.

[15] R. Bhadauria and N. Aluru, "A quasi-continuum hydrodynamic model for slit shaped nanochannel flow," *The Journal of chemical physics*, vol. 139, no. 7, p. 074109, 2013.

[16] B. A. Dalton, P. J. Daivis, J. S. Hansen, and B. Todd, "Effects of nanoscale density inhomogeneities on shearing fluids," *Physical Review E*, vol. 88, no. 5, p. 052143, 2013.

[17] B. K. Peterson, K. E. Gubbins, G. S. Heffelfinger, U. M. B. Marconi, and F. van Swol, "Lennard-jones fluids in cylindrical pores: Nonlocal theory and computer simulation," *The Journal of chemical physics*, vol. 88, no. 10, pp. 6487–6500, 1988.

[18] R. Qiao and N. Aluru, "Ion concentrations and velocity profiles in nanochannel electroosmotic flows," *The Journal of chemical physics*, vol. 118, no. 10, pp. 4692–4701, 2003.

[19] R. Qiao and N. Aluru, "Charge inversion and flow reversal in a nanochannel electro-osmotic flow," *Physical review letters*, vol. 92, no. 19, p. 198301, 2004.

[20] D. Frenkel and B. Smit, *Understanding molecular simulation: from algorithms to applications*. Academic press, 2001, vol. 1.

[21] B. Hess, C. Kutzner, D. Van Der Spoel, and E. Lindahl, "Gromacs 4: algorithms for highly efficient, load-balanced, and scalable molecular simulation," *Journal of chemical theory and computation*, vol. 4, no. 3, pp. 435–447, 2008.

[22] H. J. Berendsen, J. P. M. Postma, W. F. van Gunsteren, A. DiNola, and J. Haak, "Molecular dynamics with coupling to an external bath," *The Journal of chemical physics*, vol. 81, no. 8, pp. 3684–3690, 1984.

[23] S. Nosé, "A unified formulation of the constant temperature molecular dynamics methods," *The Journal of chemical physics*, vol. 81, no. 1, pp. 511–519, 1984.

[24] D. Fincham, "Choice of timestep in molecular dynamics simulation," *Computer physics communications*, vol. 40, no. 2, pp. 263–269, 1986.

[25] R. Evans, "Density functional theory for inhomogeneous fluids i: Simple fluids in equilibrium," *Lecture Notes at 3rd Warsaw School of Statistical Physics, Kazimierz Dolny*, vol. 27, p. 43, 2009.

[26] H. C. Andersen, "Molecular dynamics simulations at constant pressure and/or temperature," *The Journal of chemical physics*, vol. 72, no. 4, pp. 2384–2393, 1980.

[27] H. Tanaka, K. Nakanishi, and N. Watanabe, "Constant temperature molecular dynamics calculation on lennard-jones fluid and its application to watera)," *The Journal of Chemical Physics*, vol. 78, no. 5, pp. 2626–2634, 1983.

[28] K. Dill and S. Bromberg, *Molecular driving forces: statistical thermodynamics in biology, chemistry, physics, and nanoscience*. Garland Science, 2010.

[29] E. Spohr, A. Trokhymchuk, and D. Henderson, "Adsorption of water molecules in slit pores," *Journal of Electroanalytical Chemistry*, vol. 450, no. 2, pp. 281–287, 1998.

[30] H. Eslami, F. Mehdipour, A. Setoodeh, and J. Rouzegar, "Nanoconfined polymers: modelling and simulation approaches," *Molecular Simulation*, vol. 41, no. 5-6, pp. 367–381, 2015.

[31] J. D. Weeks, D. Chandler, and H. C. Andersen, "Role of repulsive forces in determining the equilibrium structure of simple liquids," *The Journal of Chemical Physics*, vol. 54, no. 12, pp. 5237–5247, 1971.

[32] T. Sanghi and N. Aluru, "A transferable coarse-grained potential to study the structure of confined, supercritical lennard-jones fluids," *The Journal of chemical physics*, vol. 132, no. 4, p. 044703, 2010.

[33] R. B. Bird, "Transport phenomena," *Applied Mechanics Reviews*, vol. 55, no. 1, pp. R1–R4, 2002.

[34] W. Humphrey, A. Dalke, and K. Schulten, "Vmd: visual molecular dynamics," *Journal of molecular graphics*, vol. 14, no. 1, pp. 33–38, 1996.

[35] S. K. Bhatia and D. Nicholson, "Modeling mixture transport at the nanoscale: Departure from existing paradigms," *Physical review letters*, vol. 100, no. 23, p. 236103, 2008.

[36] A. Raghunathan, J. Park, and N. Aluru, "Interatomic potential-based semiclassical theory for lennard-jones fluids," *The Journal of chemical physics*, vol. 127, no. 17, p. 174701, 2007.

[37] T. Sanghi and N. Aluru, "Coarse-grained potential models for structural prediction of carbon dioxide (co2) in confined environments," *The Journal of chemical physics*, vol. 136, no. 2, p. 024102, 2012.

[38] S. Mashayak and N. Aluru, "Coarse-grained potential model for structural prediction of confined water," *Journal of Chemical Theory and Computation*, vol. 8, no. 5, pp. 1828–1840, 2012.

[39] S. Mashayak and N. Aluru, "Thermodynamic state-dependent structure-based coarse-graining of confined water," *The Journal of chemical physics*, vol. 137, no. 21, p. 214707, 2012.

[40] M. S. Shell, "The relative entropy is fundamental to multiscale and inverse thermodynamic problems," *J. Chem. Phys*, vol. 129, no. 144, p. 108, 2008.

[41] C. Ebner, W. Saam, and D. Stroud, "Density-functional theory of simple classical fluids. i. surfaces," *Physical Review A*, vol. 14, no. 6, p. 2264, 1976.

[42] E. Kierlik and M. Rosinberg, "Density-functional theory for inhomogeneous fluids: adsorption of binary mixtures," *Physical Review A*, vol. 44, no. 8, p. 5025, 1991.

[43] E. Kierlik, Y. Fan, P. Monson, and M. Rosinberg, "Liquid–liquid equilibrium in a slit pore: Monte carlo simulation and mean field density functional theory," *The Journal of chemical physics*, vol. 102, no. 9, pp. 3712–3719, 1995.

[44] M. Sliwinska-Bartkowiak, R. Sikorski, S. Sowers, L. Gelb, and K. Gubbins, "Phase separations for mixtures in well-characterized porous materials: Liquid–liquid transitions," *Fluid phase equilibria*, vol. 136, no. 1, pp. 93–109, 1997.

[45] Y. Tang and J. Wu, "A density-functional theory for bulk and inhomogeneous lennard-jones fluids from the energy route," *The Journal of chemical physics*, vol. 119, no. 14, pp. 7388–7397, 2003.

[46] J. A. Barker and D. Henderson, "Perturbation theory and equation of state for fluids. ii. a successful theory of liquids," *The Journal of Chemical Physics*, vol. 47, no. 11, pp. 4714–4721, 1967.

[47] M. Wertheim, "Exact solution of the percus-yevick integral equation for hard spheres," *Physical Review Letters*, vol. 10, no. 8, p. 321, 1963.

[48] E. Thiele, "Equation of state for hard spheres," *The Journal of Chemical Physics*, vol. 39, no. 2, pp. 474–479, 1963.

[49] W. Smith and D. Henderson, "Analytical representation of the percus-yevick hard-sphere radial distribution function," *Molecular Physics*, vol. 19, no. 3, pp. 411–415, 1970.

[50] C. Caccamo, "Integral equation theory description of phase equilibria in classical fluids," *Physics reports*, vol. 274, no. 1, pp. 1–105, 1996.

[51] S. Mashayak, M. Motevaselian, and N. Aluru, "An eqt-cdft approach to determine thermodynamic properties of confined fluids," *The Journal of chemical physics*, vol. 142, no. 24, p. 244116, 2015.

[52] J. G. Kirkwood and F. P. Buff, "The statistical mechanical theory of surface tension," *The Journal of Chemical Physics*, vol. 17, no. 3, pp. 338–343, 1949.

[53] H. Eslami and N. Mehdipour, "Local chemical potential and pressure tensor in inhomogeneous nanoconfined fluids," *The Journal of chemical physics*, vol. 137, no. 14, p. 144702, 2012.

[54] R. Hartkamp, A. Ghosh, T. Weinhart, and S. Luding, "A study of the anisotropy of stress in a fluid confined in a nanochannel," *The Journal of chemical physics*, vol. 137, no. 4, p. 044711, 2012.

[55] M. Barisik and A. Beskok, "Equilibrium molecular dynamics studies on nanoscale-confined fluids," *Microfluidics and nanofluidics*, vol. 11, no. 3, pp. 269–282, 2011.

[56] J. Henderson and F. van Swol, "On the interface between a fluid and a planar wall: theory and simulations of a hard sphere fluid at a hard wall," *Molecular Physics*, vol. 51, no. 4, pp. 991–1010, 1984.

[57] F. van Swol and J. Henderson, "Wetting and drying transitions at a fluid-wall interface: Density-functional theory versus computer simulation," *Physical Review A*, vol. 40, no. 5, p. 2567, 1989.

[58] J.-P. Hansen and I. R. McDonald, "Chapter 4 - distribution function theories," in *Theory of Simple Liquids (Fourth Edition)*, J.-P. Hansen and I. R. McDonald, Eds. Oxford: Academic Press, 2013, pp. 105–147.

[59] P. B. Balbuena, D. Berry, and K. E. Gubbins, "Solvation pressures for simple fluids in micropores," *The Journal of Physical Chemistry*, vol. 97, no. 4, pp. 937–943, 1993.

[60] J. Z. Wu, "Density functional theory for liquid structure and thermodynamics," in *Molecular Thermodynamics of Complex Systems*, ser. Structure and Bonding, X. Lu and Y. Hu, Eds. Springer Berlin Heidelberg, Jan. 2009, no. 131, pp. 1–73.

[61] Y. Rosenfeld, "Free-energy model for the inhomogeneous hard-sphere fluid mixture and density-functional theory of freezing," *Physical Review Letters*, vol. 63, no. 9, pp. 980–983, Aug. 1989.

[62] Y. Rosenfeld, "Free energy model for inhomogeneous fluid mixtures: Yukawacharged hard spheres, general interactions, and plasmas," *The Journal of Chemical Physics*, vol. 98, no. 10, pp. 8126–8148, May 1993.

[63] Y. Rosenfeld, M. Schmidt, H. Lwen, and P. Tarazona, "Fundamental-measure free-energy density functional for hard spheres: Dimensional crossover and freezing," *Physical Review E*, vol. 55, no. 4, pp. 4245–4263, Apr. 1997.

[64] P. Tarazona and Y. Rosenfeld, "From zero-dimension cavities to free-energy functionals for hard disks and hard spheres," *Physical Review E*, vol. 55, no. 5, pp. R4873–R4876, May 1997.

[65] R. Roth, R. Evans, A. Lang, and G. Kahl, "Fundamental measure theory for hard-sphere mixtures revisited: the white bear version," *Journal of Physics: Condensed Matter*, vol. 14, no. 46, p. 12063, Nov. 2002.

[66] Y.-X. Yu and J. Wu, "Structures of hard-sphere fluids from a modified fundamental-measure theory," *The Journal of Chemical Physics*, vol. 117, no. 22, pp. 10 156–10 164, Nov. 2002.

[67] G. J. Gloor, G. Jackson, F. J. Blas, E. M. d. Ro, and E. d. Miguel, "An accurate density functional theory for the vapor-liquid interface of associating chain molecules based on the statistical associating fluid theory for potentials of variable range," *The Journal of Chemical Physics*, vol. 121, no. 24, pp. 12 740–12 759, Dec. 2004.

[68] G. J. Gloor, G. Jackson, F. J. Blas, E. M. del Ro, and E. de Miguel, "Prediction of the VaporLiquid interfacial tension of nonassociating and associating fluids with the SAFT-VR density functional theory," *The Journal of Physical Chemistry C*, vol. 111, no. 43, pp. 15 513–15 522, Nov. 2007.

[69] J. Hughes, E. J. Krebs, and D. Roundy, "A classical density-functional theory for describing water interfaces." *The Journal of chemical physics*, vol. 138, no. 2, pp. 024 509–024 509, Jan. 2013.

[70] P. Schofield and J. Henderson, "Statistical mechanics of inhomogeneous fluids," in *Proceedings of the Royal Society of London A: Mathematical, Physical and Engineering Sciences*, vol. 379, no. 1776. The Royal Society, 1982, pp. 231–246.

[71] "https://github.com/symashayak/gromacs/tree/release-4-6-1-localpressure_slab."

[72] J. M. Vanegas, A. Torres-Sanchez, and M. Arroyo, "Importance of force decomposition for local stress calculations in biomembrane molecular simulations," *Journal of Chemical Theory and Computation*, vol. 10, no. 2, pp. 691–702, 2014.

[73] Y. Long, J. C. Palmer, B. Coasne, M. Śliwinska-Bartkowiak, and K. E. Gubbins, "Pressure enhancement in carbon nanopores: a major confinement effect," *Physical Chemistry Chemical Physics*, vol. 13, no. 38, pp. 17 163–17 170, 2011.

[74] J. Klein and E. Kumacheva, "Confinement-induced phase transitions in simple liquids," *Science*, vol. 269, no. 5225, pp. 816–819, 1995.

[75] M. Heuberger, M. Zäch, and N. Spencer, "Density fluctuations under confinement: when is a fluid not a fluid?" *Science*, vol. 292, no. 5518, pp. 905–908, 2001.

[76] I. Snook and W. Van Megen, "Solvation forces in simple dense fluids. i," *The Journal of Chemical Physics*, vol. 72, no. 5, pp. 2907–2913, 1980.

[77] S. K. Das, M. M. Sharma, and R. S. Schechter, "Solvation force in confined molecular fluids using molecular dynamics simulation," *The Journal of Physical Chemistry*, vol. 100, no. 17, pp. 7122–7129, 1996.

[78] M. Gallo, T. M. Nenoff, and M. C. Mitchell, "Selectivities for binary mixtures of hydrogen/methane and hydrogen/carbon dioxide in silicalite and ets-10 by grand canonical monte carlo techniques," *Fluid phase equilibria*, vol. 247, no. 1, pp. 135–142, 2006.

[79] R. F. Cracknell, D. Nicholson, S. R. Tennison, and J. Bromhead, "Adsorption and selectivity of carbon dioxide with methane and nitrogen in slit-shaped carbonaceous micropores: simulation and experiment," *Adsorption*, vol. 2, no. 3, pp. 193–203, 1996.

[80] B. Coasne, J. Czwartos, M. Sliwinska-Bartkowiak, and K. E. Gubbins, "Freezing of mixtures confined in silica nanopores: experiment and molecular simulation," *The Journal of chemical physics*, vol. 133, no. 8, p. 084701, 2010.